
Validation of a discontinuous Galerkin based compressible CFD solver

Validierung eines auf der diskontinuierlichen Galerkin-Methode basierenden kompressiblen Strömungslösers

Bachelor-Thesis, Lawrence F Ayers IV

November 2015



TECHNISCHE
UNIVERSITÄT
DARMSTADT

fdy

Validation of a discontinuous Galerkin based compressible CFD solver

Validierung eines auf der diskontinuierlichen Galerkin-Methode basierenden kompressiblen Strömungslösers

Bachelor-Thesis by Lawrence Ayers

Supervisors

Prof. Dr.-Ing. habil. Martin Oberlack

Fachgebiet für Strömingsdynamik

Dipl.-Ing. Stephan Krämer-Eis

Fachgebiet für Strömingsdynamik

Conducted at

Fachgebiet für Strömingsdynamik

Technische Universität Darmstadt

Hochschulstraße 1

64289 Darmstadt

Thesis Statement

Hiermit versichere ich, die vorliegende Bachelorthesis ohne Hilfe Dritter nur mit den angegebenen Quellen und Hilfsmitteln angefertigt zu haben. Sämtliche aus fremden Quellen indirekt oder direkt übernommenen Gedanken sind als solche kenntlich gemacht. Diese Arbeit hat in gleicher oder ähnlicher Form noch keiner Prüfungsbehörde vorgelegen und wurde noch nicht veröffentlicht.

I herewith formally declare that I have written the submitted bachelor thesis independently. I did not use any outside support except for the quoted literature and other sources mentioned in the paper. I clearly marked and separately listed all of the literature and all of the other sources which I employed when producing this academic work, either literally or in content. This thesis has not been handed in or published before in the same or similar form.

In the submitted thesis the written copies and the electronic version are identical in content

Ort, Datum

Name, Vorname

Aufgabenstellung

Diese Seite wird durch die Aufgabenstellung (im Original) ersetzt.

Diese Seite ist optional,
sie kann auch nach dem
Literaturverzeichnis

Abstract

The Chair of Fluid Dynamics at TU Darmstadt has developed and validated a CFD solver called BoSSS (Bounded support spectral solver) which utilizes the discontinuous Galerkin method (DG) to solve the partial differential equations of the Navier-Stokes equations. The goal here is to validate an extension of BoSSS, which uses DG to solve the compressible, viscous Navier-Stokes equations (CNS). To do this, simulations are conducted for both steady and unsteady flows at Reynolds numbers 20, 40, 100, and 200 on a two-dimensional grid. These simulations are conducted on grids with varying numbers of elements at various levels of DG order. These results are compared with data collected from previous numerical and experimental work through use of various dimensionless values commonly used in the field. These include the wave separation length used for steady flows, the Strouhal number for unsteady flows, and coefficients of lift and drag for both. These results prove that this CNS extension is indeed accurate and valid for laminar, steady and unsteady fluid flows.

Contents

Thesis Statement.....	ii
Aufgabenstellung	iii
Abstract.....	iv
Contents.....	v
Nomenclature.....	vi
1 Introduction.....	1
1.1 State of the art	1
2 Fundamentals	3
2.1 Compressible Navier-Stokes equations	3
2.2 Dimensionless measures.....	4
3 Formulation	6
3.1 The discontinuous Galerkin method.....	6
3.1.1 Spatial discretization.....	6
3.1.2 Discretization of the viscous terms	7
3.2 Curved elements.....	9
3.3 Temporal discretization.....	12
4 Simulation properties.....	14
4.1 Dimensionless values.....	14
4.2 Simulation parameters	15
4.3 Mesh selection.....	15
5 Validation of BoSSS for compressible steady flow ($Re \leq 40$).....	19
5.1 Simulation at $Re=20$	20
5.2 Simulation at $Re=40$	22
6 Validation of BoSSS for unsteady flow ($Re > 40$)	25
6.1 Simulation at $Re=100$	26
6.2 Simulation at $Re=200$	29
7 Conclusion	34
8 Appendix.....	35
List of Figures.....	37
List of Tables	38
Bibliography.....	39

Nomenclature

P	order number	
e	solution error	
Re	Reynolds number	
Ω	domain	
Ω_h	discretized domain	
\mathbf{x}, \vec{x}	Cartesian coordinate vector	
$\vec{\xi}$	reference coordinate vector	
U	conserved flow variables	
F_c	convective flux vector	$\left[\frac{kg}{m^2 \cdot s} \right]$
F_v	viscous flux vector	$\left[\frac{kg}{m^2 \cdot s} \right]$
ρ	density	$\left[\frac{kg}{m^3} \right]$
p	pressure	$\left[\frac{N}{m^2} \right]$
\mathbf{m}	momentum vector	$\left[\frac{kg}{m^2 \cdot s} \right]$
\mathbf{u}	velocity vector	$\left[\frac{m}{s} \right]$
E	energy per unit mass	$\left[\frac{J}{kg} \right]$
T	temperature	$[K]$
κ	thermal conductivity	$\left[\frac{kg \cdot m}{s^3 \cdot K} \right]$
τ	viscous stress tensor	$\left[\frac{N}{m^2} \right]$
γ	specific heat ratio	
$\delta_{i,j}$	Kronecker delta	
μ	dynamic viscosity	$\left[\frac{kg}{m \cdot s} \right]$

L	characteristic length	$[m]$
V_∞	reference velocity	$\left[\frac{m}{s}\right]$
t	time	$[s]$
Pr	Prandtl number	
R	ideal gas constant	$\left[\frac{J}{K \cdot mol}\right]$
$c_{p,v}$	specific heat and for constant pressure and volume	$\left[\frac{J}{K \cdot mol}\right]$
\mathcal{K}_i	element defined within domain	
e_i	edge defined to element \mathcal{K}_i	
$\Phi_{i,j}$	basis/Ansatz function and test function	
\tilde{U}	global solution for U	
f	convective flux function	
$G(U)$	homogeneity tensor	
\mathbf{n}	normal vector	
$\hat{\underline{\sigma}}$	viscous SIPG flux form	
T_h	set of discretized elements	
h	discretization resolution; smallest element size of mesh	
$\delta(U^h)$	SIPG penalization term	
Γ_I	set of internal edges	
Γ	set of boundary edges	
N_v^h	solution to discretization of viscous terms	
k_L	number of control point in an element transformation	
T_L	transformation function	
$J_{i,j}$	Jacobian of a transformation	
a_l	scaling factor	
k_{1-4}	coefficients in an explicit time stepping method	

\underline{u}	max velocity	$\left[\frac{m}{s}\right]$
a	speed of sound	$\left[\frac{m}{s}\right]$
λ	blockage ratio	
q	dynamic pressure	$\left[\frac{N}{m^2}\right]$
C_L	lift coefficient	
C_D	drag coefficient	
M	Mach number	
St	Strouhal number	
W^*	Wake Separation Length	
DG	Discontinuous Galerkin Method	
CFD	Computational Fluid Dynamics	
PDE	partial differential equation	
BoSSS	Bounded Support Spectral Solver	
2D	2-dimensional	
3D	3-dimensional	
FEM	Finite Element Method	
FDM	Finite Difference Method	
FVM	Finite Volume Method	
RK4	Runge-Kutta 4 th order	
CFL	Courant-Friedrichs-Levy	
SIPG	Symmetric Interior Penalty Galerking	
HLLC	Harten Lax van Leer Contact	
BC	boundary condition	
DG1E1	discontinuous Galerkin order 1, element curvature order 1	
DG2E2	discontinuous Galerkin order 2, element curvature order 2	
DG3E3	discontinuous Galerkin order 3, element curvature order 3	

MP	mesh parameter
BC/IC	boundary condition/initial condition
CNS	compressible Navier-Stokes

1 Introduction

The chair for fluid dynamics at TU Darmstadt has been developing a program called BoSSS (Bounded Support Spectral Solver) used for solving the partial differential equations (PDEs) defining compressible fluid flow. Currently, an extension to BoSSS is being developed to solve the Euler equations of the compressible Navier-Stokes equations that contain the fluid's viscous terms. The goal of this thesis is to validate this developing extension by comparing its simulation results with various baseline data from numerical simulations and experiments in the field.

The method used in BoSSS to solve these spatial partial differential equations is called the discontinuous Galerkin method (DG), which is a high order technique growing popularity in the field of computational fluid dynamics (CFD). High-order techniques are known for their higher accuracy and lower expense than that of low-order methods, that often have difficulties in delivering asymptotically grid converged solutions. Here, the order of a method is given by P for $e \propto h^P$, where e is the solution error and h is the mesh size. It is considered within the Fluid Dynamics community that “high order” is specific to methods that are “third order or higher”, i.e. $k \geq 3$, as stated in Wang et al. [2012]. The temporal aspect of the compressible Navier-Stokes equation will be solved using an explicit, 4th order Runge-Kutta method due to its high computational efficiency.

In this work, BoSSS will simulate the fluid flow around a circular cylinder at increasing Reynolds numbers in a two-dimensional domain. The meshes used are composed of quadrilateral elements of various curvatures (element order) on a grid, and are simulated at various orders of the DG method (DG order). It is important to use curved boundary elements for high order schemes so that an overall high accuracy solution can be delivered.

As the Reynolds number is increased in these simulations, the flow in the wake of the cylinder will transition from a steady-state flow (time invariant), to a vortex shedding flow known as the von Kármán vortex street.

1.1 State of the art

The compressible, viscous flow examined around a circular cylinder exhibits unique properties in its wake within specific ranges of Reynolds numbers. These phenomena include steady, transitional, and unsteady flows, where measures like the lift coefficient, drag coefficient, base suction coefficient, and Strouhal St number are used to characterize their behavior. The presences of instabilities in the wake vary in 2 and 3 dimensions (2D and 3D) depending on the value of the Reynolds number. For purposes for validating BoSSS, only 2D laminar flows within $0 < Re \leq 200$ will be examined in this thesis.

Persillon and Braza [1998] state that the first published experimental studies on the subject of flow regimes were conducted by Roshko in [1954], where he separated 3 different ranges of Reynolds numbers for flow in the wake of a cylinder. Roshko defined these as the laminar, transition, and irregular turbulent regimes for low to moderately-low Reynolds numbers. He found that the transition regime had distinct irregularities in the velocity fluctuation in the wake of the cylinder.

In the experimental work by Williamson [1996], these ranges are split into “vortex shedding regimes”, where flows of $Re < 49$ are in the laminar steady regime, $Re = 49$ to $140 - 194$ are in the laminar vortex shedding regime, and $Re \sim 190$ to 260 are in the wake-transition regime. The steady regime contains two symmetrical vortices on both sides of the wake that act independent of time after the flow has reached steady state (Fig 1.1, a). The shedding regime marks the start of instabilities in the wake, where vortices oscillate periodically in a von Kármán vortex street (Fig1.1, b).

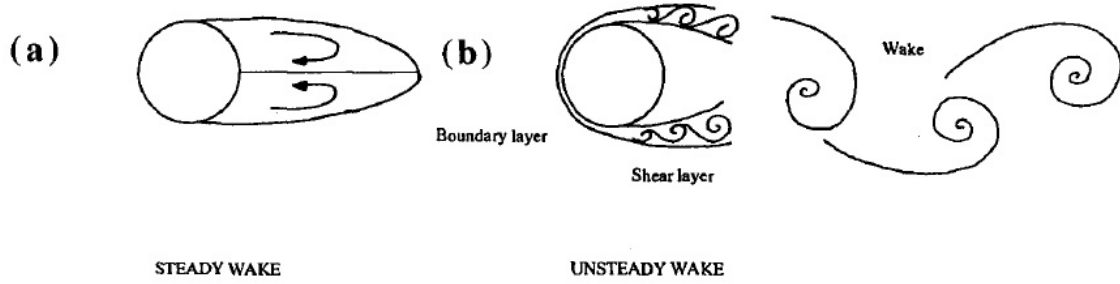


Figure 1.1: steady and unsteady wakes behind a circular cylinder, taken from Williamson [1996]

In comparison to Williamson, Anderson [2001] defines the steady flow regime as $4 < Re < 40$ and unsteady regime as flows above $Re = 40$ for incompressible viscous flow in the wake.

In one of the first numerical studies of the subject from Gresho et al. [1984], it is found that the flow's stable regime takes place up to $Re = 50$ for all initial perturbations. Here it becomes clear that an excitation in the flow, e.g. initially generating an instantaneous vortex or moving the cylinder slightly, must take place in numerical solutions to initiate vortex shedding in the wake. This is confirmed in the work by Braza et al. [1986], who is unable to witness vortex shedding in the wake until $Re = 1000$ without using an initial perturbation. This can also be seen in the works of Saiki and Biringen [1996] and Noack and Eckelmann [1994], who define the stable flow regime as up to $Re = 54$ for all perturbations.

In the earlier experimental work from Williamson [1989], and referenced by Zdravkovich [1996], 3D disturbances in the wake are said to begin at $Re = 180$ and grow with increasing Reynolds number. Williamson [1996] later defines the presence 3D instabilities in the flow at a Reynolds number of $Re \geq 260$, that occur from shear forces in the wake. In the results from the low-order Galerkin simulations conducted by Noack and Eckelmann [1994] it is shown that 3D disturbances begin at $Re = 170$. A comparison of 2D and 3D simulations conducted by Persillon and Braza [1998], found that flow values for $Re = 100$ were the same in two and three dimensions, while the $Re = 200$ values showed little differences. It was therefore determined that the simulations in this thesis could run accurately in two dimensions up to $Re = 100$, and fairly accurately up to $Re = 200$.

2 Fundamentals

2.1 Compressible Navier-Stokes equations

The Navier-Stokes equation is used in this thesis to define the flow properties of compressible, viscid fluid flow. It does this by utilizing the conservation laws for mass, momentum, and energy. The derivation of the compressible Navier-Stokes equation (CNS) is examined in detail by Anderson [2001].

The two-dimensional Compressible Navier-Stokes equation,

$$\frac{\partial U}{\partial t} + \left(\frac{\partial F_c^x(U)}{\partial x} + \frac{\partial F_c^y(U)}{\partial y} \right) - \left(\frac{\partial F_v^x(U, \nabla U)}{\partial x} + \frac{\partial F_v^y(U, \nabla U)}{\partial y} \right) = 0 \text{ for } x, y \in \Omega, \quad (2.1)$$

is separated into three elements; the temporal derivative of the conserved flow variables U , and the spatial derivatives of the convective F_c and viscous F_v fluxes as functions of U and ∇U .

$$U = \begin{pmatrix} \rho \\ \rho u \\ \rho v \\ \rho E \end{pmatrix}, F_c^x = \begin{pmatrix} \rho u \\ \rho u^2 + p \\ \rho uv \\ (\rho E + p)v \end{pmatrix}, F_c^y = \begin{pmatrix} \rho v \\ \rho uv \\ \rho v^2 + p \\ (\rho E + p)u \end{pmatrix}, \quad (2.2)$$

$$F_v^x = \begin{pmatrix} 0 \\ \tau_{xx} \\ \tau_{xy} \\ u\tau_{xx} + v\tau_{xy} + \kappa \frac{\partial T}{\partial x} \end{pmatrix}, F_v^y = \begin{pmatrix} 0 \\ \tau_{xy} \\ \tau_{yy} \\ u\tau_{xy} + v\tau_{yy} + \kappa \frac{\partial T}{\partial y} \end{pmatrix}$$

In vector U , ρ is the fluid density, $\mathbf{m} = (\rho u, \rho v)^T$ is the momentum vector that contains the velocity vector $\mathbf{u} = (u, v)^T$, and ρE is the total energy per volume. In the convective and viscous fluxes, p is the pressure, E is the energy per unit mass, κ is the thermal conductivity, and T is the temperature of the system. The pressure is determined by using the ideal gas equation of state

$$p = (\gamma - 1)(\rho e) \quad (2.3)$$

that has a specific heat ratio $\gamma = 1.4$ and an internal energy ρe specific to the system. The viscous terms are denoted in Einstein notation as

$$\tau_{ij} = \mu \left[\left(\frac{\partial u_i}{\partial x_j} + \frac{\partial u_j}{\partial x_i} \right) - \frac{2}{3} \frac{\partial u_k}{\partial x_k} \delta_{ij} \right], \quad (2.4)$$

where i and j refer to the elements in the Cartesian coordinate vector $\mathbf{x} = (x, y)^T$, and k refers to the sum of these two values. δ_{ij} is the Kronecker delta that produces the binary result

$$\delta_{ij} = \begin{cases} 0 & \text{if } i \neq j \\ 1 & \text{if } i = j \end{cases} \quad (2.5)$$

such that indices of different value generate zero terms. The viscous shear forces of the fluid are introduced through the dynamic viscosity μ , which is not constant but rather dependent on the temperature T using the power law or Sutherland's law,

$$\mu = \mu(T) = T^\omega \text{ or } \mu(T) = T^{3/2} \left(\frac{1 + S/T_\infty}{T + S/T_\infty} \right), \quad (2.6)$$

where ω is the viscosity exponent and S is the Sutherland constant.

Without making assumptions about the system, i.e. constant density, it is impossible to solve these partial differential equations analytically. Therefore, it is necessary to solve these using a numerical solution like the discontinuous Galerkin method.

2.2 Dimensionless measures

The values used in these equations take on a dimensionless form so that results can be easily transferred between small, model and large, real life scenarios. The following reference quantities are defined. For an arbitrary system, L_∞ is a reference length, V_∞ is a reference velocity, ρ_∞ is a reference density, μ_∞ is a reference viscosity and κ_∞ is a reference thermal conductivity coefficient. As seen in the work done by Feistauer et al. [2003], any other reference quantities can all be derived from these basic ones, t from L_∞/u_∞ , p and ρE from $\rho_\infty V_\infty^2$, to form the dimensionless quantities,

$$\begin{aligned} t^* &= \frac{V_\infty}{L_\infty} \cdot t, & x_i^* &= \frac{1}{L_\infty} \cdot x_i, & u_i^* &= \frac{1}{V_\infty} \cdot u_i, \\ p^* &= \frac{1}{\rho_\infty V_\infty^2} \cdot p, & \mu^* &= \frac{1}{\mu_\infty} \cdot \mu, & \kappa^* &= \frac{1}{\kappa_\infty} \cdot \kappa, \\ \rho^* &= \frac{1}{\rho_\infty} \cdot \rho, & \rho E^* &= \frac{1}{\rho_\infty V_\infty^2} \cdot \rho E, & T^* &= \frac{R}{V_\infty^2} \cdot T, \end{aligned} \quad (2.7)$$

and the corresponding operators, e.g. derivatives,

$$\begin{aligned} \frac{\partial}{\partial t} &= \frac{\partial t^*}{\partial t} \frac{\partial}{\partial t^*} = \frac{V_\infty}{L_\infty} \frac{\partial}{\partial t^*}, \\ \frac{\partial}{\partial x_i} &= \frac{\partial x_i^*}{\partial x_i} \frac{\partial}{\partial x_i^*} = \frac{1}{L_\infty} \frac{\partial}{\partial x_i^*}, \\ \nabla &= \frac{1}{L_\infty} \nabla^*. \end{aligned} \quad (2.8)$$

By plugging in these dimensionless quantities into the continuity, momentum, and energy equations,

$$\begin{aligned} \frac{\partial \rho}{\partial t} + \frac{\partial(\rho u_i)}{\partial x_i} &= 0, \\ \frac{\partial \rho u_i}{\partial t} + \frac{\partial \rho u_i u_j}{\partial x_j} + \frac{\partial p}{\partial x_i} &= \frac{\partial \tau_{ij}}{\partial x_i}, \\ \frac{\partial \rho E}{\partial t} + \frac{\partial \rho E u_i}{\partial x_i} + \frac{\partial p u_i}{\partial x_i} &= \frac{\partial \tau_{ij} u_j}{\partial x_i} + \frac{\partial}{\partial x_i} \left(\kappa \frac{\partial T}{\partial x_i} \right), \end{aligned} \quad (2.9)$$

as seen by Feistauer et al. pg 38 [2003], the following dimensionless quantities can be derived.

$$\begin{aligned} Re &= \frac{\rho_\infty V_\infty L_\infty}{\mu_\infty} \propto \frac{\text{inertia forces}}{\text{viscous forces}} \\ Pr &= \frac{\mu_\infty c_p}{k_\infty} \propto \frac{\text{viscous diffusion rate}}{\text{thermal diffusion rate}} \end{aligned} \quad (2.10)$$

The ideal gas law states

$$\gamma = \frac{c_p}{c_v} \text{ and } R = c_p - c_v, \quad (2.11)$$

where R is the ideal gas constant, and c_p and c_v are the specific heats for constant pressure and volume. These dimensionless values are then placed back into the original Navier-Stokes equations to get the dimensionless viscous fluxes

$$F_v^x = \frac{1}{Re} \begin{pmatrix} 0 \\ \tau_{xx} \\ \tau_{xy} \\ u\tau_{xx} + v\tau_{xy} + \kappa \frac{\gamma}{Pr(\gamma-1)} \frac{\partial T}{\partial x} \end{pmatrix}, F_v^y = \frac{1}{Re} \begin{pmatrix} 0 \\ \tau_{xy} \\ \tau_{yy} \\ u\tau_{xy} + v\tau_{yy} + \kappa \frac{\gamma}{Pr(\gamma-1)} \frac{\partial T}{\partial y} \end{pmatrix}. \quad (2.12)$$

From here on forward in this thesis, all values mentioned can be assumed to be dimensionless since they are the only variables used in the BoSSS simulations.

3 Formulation

3.1 The discontinuous Galerkin method

The discontinuous Galerkin method is a numerical method used to calculate the partial differential equations that define fluid flow properties. Primarily, these practices used today can be broken down into three categories: the finite difference method (FDM), the finite volume method (FVM), and the finite element method (FEM). All of these methods place the fluid into some sort of grid-like-structure in space, but solve the associated partial differential equations differently.

The discontinuous Galerkin method uses both the finite element and finite volume methods to solve these partial differential equations and will be described below in its conjuncture with BoSSS. A short description of DG and the validation of various aspects of BoSSS are also investigated in the masters theses of Utz [2014] and Fischer [2014]. An in-depth description of DG can be found in publications by Hesthaven and Warburton [2008], and the Ph.D. dissertation from Müller [2014].

The Navier-Stokes equation (2.1) will now be broken into its three separate parts as to individually solve the temporal derivative, the convective fluxes, and the viscous fluxes. The temporal aspect is solved using an explicit 4th order Runge Kutta scheme, while the fluxes are solved using the discontinuous Galerkin method.

3.1.1 Spatial discretization

Examining only the first two terms of the compressible Navier-Stokes equations, an example will be given using a one dimensional form of the scalar conservation law,

$$\frac{\partial U}{\partial t} + \frac{\partial F_c(U)}{\partial x} = 0, \quad (3.1)$$

where U holds the flow values being conserved, and the $F_c(U)$ is the convective flux of this value in the direction x . This equation states that U entering and exiting the domain Ω is equal and independent of time or space. The domain, Ω will be divided into $\{\mathcal{K}_i\}_{i=1,2,3\dots N}$ sub-elements each consisting of left ($e_{i,L}$) and right edges ($e_{i,R}$) on a one-dimensional (1D) number line, where \mathcal{K}_i is arbitrary element on this line, as seen in fig 3.1. This new discretized domain will be denoted as Ω_h .

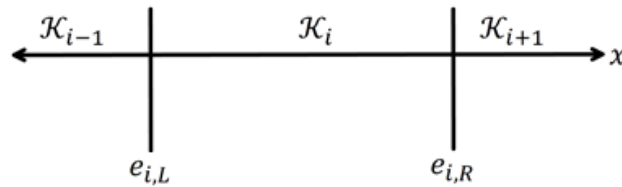


Figure 3.1: 1D element discretization of elements \mathcal{K}_{i-1} , \mathcal{K}_{i-1} , and \mathcal{K}_i with corresponding edges

Like that of the FEM, DG also defines basis or ansatz functions $\{\Phi_{i,j}\}_{j=1,2,3\dots M}$ across each element. Chosen for this case are modal functions containing orthonormal polynomials set to degree P . These are used to achieve a solution for U by means of the global solution \tilde{U} (3.2) seen below.

$$U(x, t)|_{\mathcal{K}_i} \approx \tilde{U}(x, t)|_{\mathcal{K}_i} = U_i(x, t) = \sum_{k=0}^M U_{i,k}(t) \Phi_{i,k}(x) \quad (3.2)$$

There are M number of ansatz functions $\Phi_{i,j}$ and coefficients U_i that are defined locally to each element. These coefficients and their corresponding ansatz functions are added together to make the approximate local solution $U_i(x, t)$, i.e. the global solution \tilde{U} , at element \mathcal{K}_i . However, this solution is not continuous across the element boundaries in Ω_h ,

$$\begin{aligned} \lim_{x \in \mathcal{K}_{i-1} \rightarrow e_{i,L}} U(x) &:= U_{i,L}^+ \neq U_{i,L}^- := \lim_{x \in \mathcal{K}_i \rightarrow e_{i,L}} U(x) \text{ and} \\ \lim_{x \in \mathcal{K}_i \rightarrow e_{i,R}} U(x) &:= U_{i,R}^+ \neq U_{i,R}^- := \lim_{x \in \mathcal{K}_{i+1} \rightarrow e_{i,R}} U(x), \end{aligned} \quad (3.3)$$

where x is defined as a value within \mathcal{K}_{i-1} approaching the boundary $e_{i,L}$ on the left side of the equation, and x is defined as a value within \mathcal{K}_i approaching the internal boundary $e_{i-1,R}$.

Therefore, the FVM of using numerical flux functions is utilized to generate continuous values at these boundaries. Here, the variables used are defined so that the flux function at these boundary, is

$$f(U_{i,L}^+, U_{i,L}^-) = -f(U_{i,R}^+, U_{i,R}^-). \quad (3.4)$$

For purposes of this explanation, the simplest, Rusanov (or *local* Lax-Friedrichs), numerical flux function is used,

$$f(U_{i,L}^+, U_{i,L}^-) = \frac{F_c(U_{i,L}^+) + F_c(U_{i,L}^-)}{2} \text{ and } f(U_{i,R}^+, U_{i,R}^-) = \frac{F_c(U_{i,R}^+) + F_c(U_{i,R}^-)}{2}, \quad (3.5)$$

that defines these discontinuities or “jumps” as the average of the two flux values involved at these boundaries. In the BoSSS simulation validated in this thesis, however, the well-known Harten Lax van Leer Contact (HLLC) flux function is used. First introduced by Toro [1989], the HLLC flux is tailored to ideal gases and is known to be very efficient. For more information, see the works of Toro [2009] and LeVeque [1992].

In accordance with the Galerkin method, the modal approximation ansatz functions $\Phi_{i,j}$ are used again as the test functions in the discrete weak formulation of the original equation (3.1),

$$\int_{x_{i,L}}^{x_{i,R}} \left[\frac{\partial U}{\partial t} \Phi_{i,j} + \frac{\partial F_c(U)}{\partial x} \Phi_{i,j} \right] dx = 0. \quad (3.6)$$

Like the ansatz functions, these test functions are polynomials to the degree P , which is defined as the DG order of the entire numerical solution. A higher DG order makes for a more accurate solution, but also requires more processing power and time for calculation.

Since the flux, test, and ansatz functions have been defined, these values can be plugged in to the weak formulation and be solved through integration by parts,

$$\int_{x_{i,R}}^{x_{i,L}} \frac{\partial U}{\partial t} \Phi_{i,j} dx + f(U_{i,L}^+, U_{i,L}^-) \Phi_{i,j} - f(U_{i,R}^+, U_{i,R}^-) \Phi_{i,j} - \int_{x_{i,R}}^{x_{i,L}} F(U) \frac{\partial \Phi_{i,j}}{\partial x} dx = 0. \quad (3.7)$$

This weak formulation is then solved numerically, which provides an approximate solution to the PDE with respect to the physical domain.

3.1.2 Discretization of the viscous terms

Like the convective fluxes, the viscous terms of the compressible Navier-Stokes equations are also solved using the discontinuous Galerkin method. The method used here, however, re-

quires more calculation since there are second order partial differential equations involved. The method used here can be found in the work by Hartmann and Houston [2008].

The viscous term of a two dimensional Navier-Stokes equations will be examined as follows,

$$\left(\frac{\partial F_c^x(U)}{\partial x} + \frac{\partial F_c^y(U)}{\partial y} \right) - \left(\frac{\partial F_v^x(U, \nabla U)}{\partial x} + \frac{\partial F_v^y(U, \nabla U)}{\partial y} \right) = 0 \text{ for } x, y \in \Omega, \quad (3.8)$$

or simply,

$$\nabla F_c^i(U) - \nabla F_v^i(U, \nabla U) = 0 \text{ for } x, y \in \Omega, \quad (3.9)$$

where the dimensionless viscous fluxes are defined in equation (2.12).

Here, convective fluxes can be ignored as they were solved in the prior spatial discretization, and the viscous fluxes are now explicitly examined. The system is now written with the homogeneity tensor $G(U)$, such that

$$-\nabla \cdot (G(U) \nabla U) = 0, \quad (3.10)$$

where $G(U) \nabla U = \nabla F_v^i(U, \nabla U)$. This system is converted to a first order system where

$$\begin{aligned} \underline{\sigma} &= G(U) \nabla U, \text{ and} \\ -\nabla \cdot \underline{\sigma} &= 0. \end{aligned} \quad (3.11)$$

As seen previously in the spatial discretization (3.6), this term is multiplied by a test function $\underline{\varphi}$, where $\underline{\varphi} = \nabla \Phi$. These equations (3.10 and 3.11) are integrated across the element \mathcal{K}_i by means of integration by parts,

$$\begin{aligned} \int_{\mathcal{K}_i} \underline{\sigma} : \underline{\varphi} \, d\mathbf{x} &= - \int_{\mathcal{K}_i} U \nabla \cdot (G(U) \underline{\varphi}) \, d\mathbf{x} + \int_{\partial \mathcal{K}_i} U (G(U) \underline{\varphi}) \cdot \mathbf{n} \, ds \\ \int_{\mathcal{K}_i} -\nabla \underline{\sigma} : \Phi \, d\mathbf{x} &= 0 = - \int_{\mathcal{K}_i} \underline{\sigma} : \nabla \Phi \, d\mathbf{x} + \int_{\partial \mathcal{K}_i} \underline{\sigma} \cdot \mathbf{n} \Phi \, ds \end{aligned} \quad (3.12)$$

where \mathbf{n} is defined as the normal vector over the boundary edge $\partial \mathcal{K}_i$. Since the viscous terms are defined in a 2D domain, the prior discretized domain Ω_h presented in 3.1.1 is now composed of quadrilateral elements composed of 4 edges (top e_T , bottom e_B , left e_L , right e_R). At every internal edge, there is a positive (e^+) and negative (e^-) valued side to show the outward direction, \mathbf{n}^+ and \mathbf{n}^- , of the flux and the conserved values corresponding to it.

Next, the numerical flux formulation needs to be defined by summing these flux functions over all of the elements in the discretized domain Ω_h ,

$$\begin{aligned} \int_{\Omega_h} \underline{\sigma}^h : \underline{\varphi}^h \, d\mathbf{x} &= - \int_{\Omega_h} U^h \nabla \cdot (G^T(U^h) \underline{\varphi}^h) \, d\mathbf{x} + \sum_{\mathcal{K} \in T_h} \hat{U}^h (G(U^h) \underline{\varphi}^h) \cdot \mathbf{n} \, ds \\ \int_{\Omega_h} -\nabla \underline{\sigma} : \Phi \, d\mathbf{x} &= 0 = - \int_{\Omega_h} \underline{\sigma}^h : \nabla \Phi^h \, d\mathbf{x} + \sum_{\mathcal{K} \in T_h} \int_{\Omega_h} \hat{\sigma}^h \cdot \mathbf{n} \, ds \end{aligned} \quad (3.13)$$

where the elements are organized in the set T_h , and \hat{U}^h and $\hat{\sigma}^h$ are the numerical flux functions. Like the HLLC and Rusanov flux functions seen prior with the convective fluxes, the viscous fluxes use the Symmetric Interior Penalty (SIPG) flux formulation given as,

$$\hat{U} = \{U^h\}, \hat{\sigma}^h = \{G(U^h) \nabla U^h\} - \delta(U^h), \quad (3.14)$$

that uses the penalization term $\delta(U^h)$,

$$\delta(U^h) = \delta^{ip}(U^h) = c_{IP} \frac{p^2}{h_e} \{ \{G(U^h)\} \} \llbracket U^h \rrbracket, \quad (3.15)$$

In order to eliminate the use of $\underline{\sigma}$ in the solution, and therefore reduce the problem size of the system by $(d + 1)$, a second integration of parts is performed on (equations 3.14) to form the *primal formulation*. This form represents a discretization of a first order system with the unknowns $U^h \in \mathbf{V}_p^{h,d}$ and $\underline{\sigma}^h \in \Sigma_p^{h,d}$, and will only contain the primal variable U^h . The *primal formulation* is written in a cell-based form,

$$\begin{aligned} \int_{\Omega_h} \underline{\sigma}^h : \nabla^h \Phi^h d\mathbf{x} &= \\ &= \int_{\Omega_h} G(U^h) U^h \nabla^h : \nabla^h \Phi^h d\mathbf{x} + \sum_{\mathcal{K} \in \mathcal{T}_h} (\hat{U}^h - U^h) (G^T(U^h) \nabla^h \Phi^h) \cdot \mathbf{n} ds. \end{aligned} \quad (3.16)$$

In the discretized domain, however, each element neighbors at least two other elements, which creates a system that summates two different values for the same shared edge, i.e. the discontinuities at the shared interior edges of neighboring cells. Therefore, the primal formulation (3.16) needs to be placed into a face-based form so that the internal and boundary (edges are not shared with a neighboring element) edges can be separately defined. The internal edges will be placed into a set $e \in \Gamma_i$, and the other “un-paired” boundary edges will be in a set $e \in \Gamma$. The values at these separately defined edges are placed into the mean value $\{\{\cdot\}\}$ and jump operators $\llbracket \cdot \rrbracket$,

$$\begin{aligned} \{\{\Phi\}\} &= \frac{1}{2}(\Phi^+ + \Phi^-) \text{ on } \Gamma_i, & \{\{\Phi\}\} &= \Phi^+ \text{ on } \Gamma, \\ \{\{\varphi\}\} &= \frac{1}{2}(\underline{\varphi}^+ + \underline{\varphi}^-) \text{ on } \Gamma_i, & \{\{\varphi\}\} &= \underline{\varphi}^+ \text{ on } \Gamma, \\ \llbracket \varphi \rrbracket &= \underline{\varphi}^+ \mathbf{n}^+ + \underline{\varphi}^- \mathbf{n}^- \text{ on } \Gamma_i, & \llbracket \varphi \rrbracket &= \underline{\varphi}^+ \mathbf{n}^+ \text{ on } \Gamma, \\ \llbracket \Phi \rrbracket &= \Phi^+ \otimes \mathbf{n}^+ + \Phi^- \otimes \mathbf{n}^- \text{ on } \Gamma_i, & \llbracket \Phi \rrbracket &= \underline{\Phi}^+ \otimes \mathbf{n}^+ \text{ on } \Gamma, \end{aligned} \quad (3.17)$$

as to allow for the transfer between cell-based and face-based integrals and the *face based formulation* can be defined,

$$\sum_{\mathcal{K} \in \mathcal{T}_h} (\underline{\varphi}^+ \mathbf{n}^+) \cdot \underline{\Phi}^+ ds = \int_{\Gamma_i} \{\{\varphi^h\}\} : \llbracket \Phi^h \rrbracket ds + \int_{\Gamma} \{\{\Phi^h\}\} : \llbracket \varphi^h \rrbracket ds. \quad (3.18)$$

The primal form (3.16) can now be placed into this face based formulation (3.18),

$$\begin{aligned} N_v^h(U^h, \Phi^h) &= \int_{\Omega} G(U^h) \nabla^h U^h : \nabla^h \Phi^h d\mathbf{x} - \int_{\Gamma_i} \llbracket U^h \rrbracket : \{\{G^T(U^h) \nabla^h \Phi^h\}\} ds \\ &\quad - \int_{\Gamma_i} \{\{G(U^h) \nabla^h U^h\}\} : \llbracket \Phi^h \rrbracket ds + \int_{\Gamma} \delta(U^h) : \llbracket \Phi^h \rrbracket ds + \hat{N}_F^h(U^h, \Phi^h), \end{aligned} \quad (3.19)$$

where $\hat{N}_F^h(U^h, \Phi^h)$ are the boundary terms for edges $e \in \Gamma$. For more information, see the work of Hartmann and Houston [2008].

3.2 Curved elements

When the spatial domain is composed of linear elements, i.e. elements that are shaped with straight edges, the accuracy of the high order scheme is limited to that of the accuracy of the discretized grid. It is therefore beneficial to use a high order scheme to approximate the geometry used in the simulation. The validation of using curved elements in BoSSS was investigated by Utz [2014].

The methods used here base the ansatz functions for each element on reference elements whose dimensions are mapped onto the coordinates ξ_1 and ξ_2 of the reference domain $\vec{\xi}$. Ex-

emplified in figure 3.2, this reference element $\hat{\mathcal{K}}$ is mapped onto coordinates x_1 and x_2 of the Cartesian domain \vec{x} by means of the transformation T_l ,

$$\begin{aligned}\mathcal{K}_l &= T_l(\hat{\mathcal{K}}), \\ \vec{x} &= T_l(\vec{\xi}) \text{ for } x \in \mathcal{K}_l, \\ \vec{\xi} &= T_l^{-1}(\vec{x}) \text{ for } x \in \mathcal{K}_l,\end{aligned}\tag{3.20}$$

to create the newly defined element \mathcal{K}_l . This process is known as *reference-to-physical frame mapping*, and can be further explored in the works of Botti [2012] and Hartmann and Houston [2002].

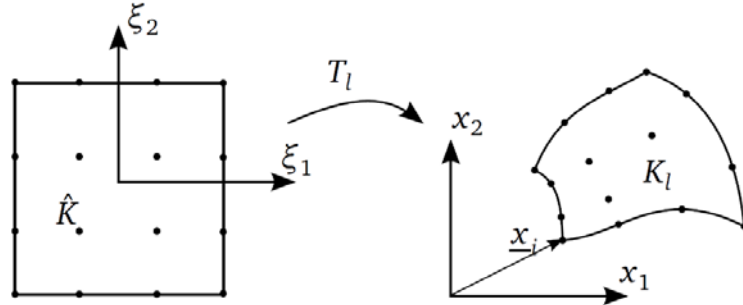


Figure 3.2: The transformation T_l used from the reference element $\hat{\mathcal{K}}$ to \mathcal{K}_l in the computational domain for a third order element, taken from Utz [2014].

The transformation uses k_L control points on each element to create edges of a desired polynomial order P , and is determined by

$$k_L = (P + 1)^D, \tag{3.21}$$

where D is the number of spatial dimensions in the domains (here it is 2). This order P will be referred to as the element order, and is always equal to that of the DG order for purposes in this thesis. Lagrange polynomials $L_i(\vec{\xi})$ are then used for the interpolation function

$$\vec{x} = \sum_{i=0}^{k_L} \vec{x}_i L_i(\vec{\xi}), \tag{3.22}$$

such that \vec{x}_i is the location of the point in the Cartesian domain \vec{x} in conjunction with the same point in the reference domain $\vec{\xi}$. Like that of the Kronecker delta, the Lagrange polynomials produce the binary result,

$$L_i(\xi_k) = \begin{cases} 0 & \text{for } k \neq i \\ 1 & \text{for } k = i \end{cases} \tag{3.23}$$

When a linear element is desired, three control points are used in the two dimensional case, as shown in figure 3.3a. This transformation is linear

$$T(\vec{\xi}) = \mathbf{T}\vec{\xi} + \vec{a}, \tag{3.24}$$

where \mathbf{T} is a 2×2 matrix that allows the system to be easily inverted, thus making for an easy transformation. In order to generate higher order polynomials, like that seen in figure 3.3c, this matrix has to be inverted numerically.

Integrating the polynomial function over the element in the physical domain is performed by first integrating over the reference element

$$\int_{\mathcal{K}_l} f(x) dx = \int_{\mathcal{K}} f(\xi) |det J_l| d\xi, \quad (3.25)$$

with the determinant of the Jacobian of the transformation J_l

$$J_{l,ij} = \frac{\partial x_l}{\partial \xi_l} \Big|_{x \in \mathcal{K}_l} = \frac{\partial T_l(\xi)_j}{\partial \xi_j}. \quad (3.26)$$

It should be noted that the Jacobian is not constant and must be solved at each of the quadrature nodes.

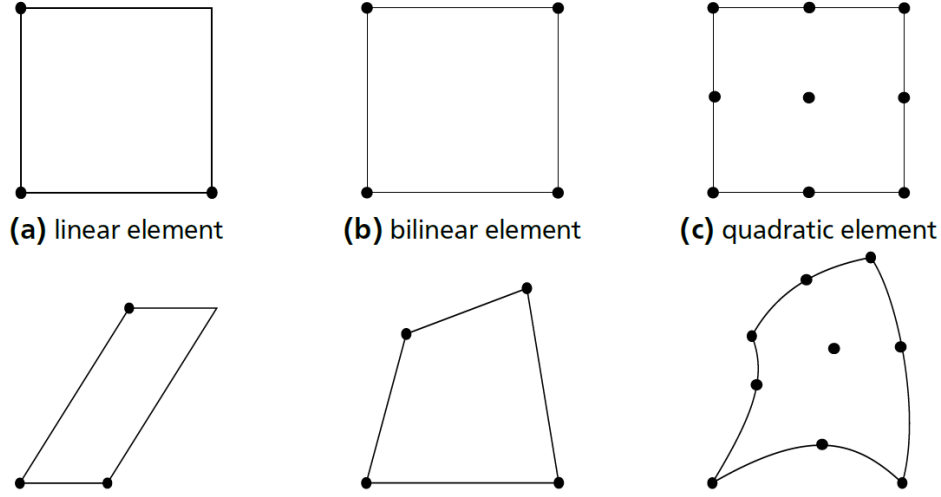


Figure 3.3: Three different possible transformations for linear, bilinear, and quadratic elements, where the top contain the elements in the reference domain and the bottom contains the elements in the Cartesian domain, taken from Utz [2014].

The orthonormal ansatz functions $\Phi_i(x)$ introduced in the spatial discretization in 3.1.1 are now defined as $\Phi_l(x)$ over the transformed 2D Cartesian element \mathcal{K}_l . These ansatz functions are a linear combination of orthonormal ansatz functions $\hat{\Phi}_n$ on the reference element

$$\Phi_{l,n}(x) = \sum_{m=0}^M (a_{l,n,m} \hat{\Phi}_m(\xi)). \quad (3.27)$$

When linear elements are desired, the scaling factor a is simply

$$a_{l,n,m} = a_{l,n,m} = \frac{1}{\sqrt{|det T_l|}} \delta_{n,m}, \quad (3.28)$$

and for curved elements the Gram-Schmidt algorithm is used, as seen in the works of mer [2012] and Botti [2012]. After the scaling factor is solved, the values in the Cartesian domain are solved as

$$\begin{aligned} U_l(\vec{x}) &= \sum_{n=0}^N U_{l,n} \Phi_{l,n}(\vec{x}) \\ &= \sum_{n=0}^N \left(U_{l,n} \sum_{m=0}^M (a_{l,n,m} \hat{\Phi}_m(\vec{\xi})) \right) = \sum_{n=0}^N \sum_{m=0}^M (U_{l,n} a_{l,n,m} \hat{\Phi}_m(T_l^{-1}(\vec{x}))) \end{aligned} \quad (3.29)$$

The method implemented by BoSSS applies the same curvature to all elements as opposed to specifically assigning different polynomial orders to the boundary and interior edges. Although mixed-order grid would speed up the numerical computation, the programming required is difficult and time-consuming to implement.

3.3 Temporal discretization

The first element, the time derivative, in the Navier-Stokes equation (2.1) is now solved using a time discretization, which is performed using a classical explicit 4th order Runge-Kutta scheme. The explicit RK4 scheme is computationally more efficient than that of implicit schemes and it is used here to solve for the steady state solution of the unsteady differential equations. An explicit method solves for the system at later time of a system U_i^{n+1} , using the system at the current time U_i^n through a number of operations that depends on order of the scheme, e.g. 4th order = 4 coefficients k_{1-4} . These methods are well known and can be found in most textbooks on the subject, like that of Schäfer [2006].

This integral is first rewritten as a system of ordinary differential equations,

$$\begin{aligned} \int_{x_{i,R}}^{x_{i,L}} \frac{\partial U}{\partial t} \Phi_{i,j} \partial x &= \int_{x_{i,R}}^{x_{i,L}} \frac{\partial}{\partial t} \left(\sum_{k=0}^M U_{i,k}(t) \Phi_{i,k}(x) \right) \Phi_{i,j} \partial x, \\ \sum_{j=0}^M \frac{\partial U_{i,j}}{\partial t} \int_{x_{i,R}}^{x_{i,L}} \Phi_{i,k} \Phi_{i,j} \partial x &= (\mathbf{M}_i)_{k,j} \frac{\partial U_i}{\partial t}, \end{aligned} \quad (3.30)$$

so that the mass matrix, \mathbf{M}_i , contains the polynomial products of the test and ansatz functions (test and ansatz functions are the same in accordance to the discontinuous Galerkin method) for the element \mathcal{K}_i . The result can be placed back into the original scalar conservation law, where f_i is the numerical flux function result found in the spatial discretization (3.7),

$$\frac{\partial U_i}{\partial t} + \mathbf{M}_i^{-1} f_i = 0, \quad (3.31)$$

and contains these orthonormal polynomials that behave such that,

$$\frac{\partial U_i}{\partial t} + f_i = 0. \quad (3.32)$$

In figure 3.4, the 4th order Butcher tableaus for the RK4 shows the values that are used with the coefficients k_{1-4} , to produce a solution for U_i at time $n + 1$,

$$\begin{aligned} \frac{U_i^{n+1} - U_i^n}{\Delta t_n} &= \frac{1}{6} (k_1 + 2k_2 + 2k_3 + k_4) \\ k_1 &= \mathbf{f}_i(U_i^n) \\ k_2 &= \mathbf{f}_i\left(U_i^n + \frac{\Delta t_n}{2} k_1\right) \\ k_3 &= \mathbf{f}_i\left(U_i^n + \frac{\Delta t_n}{2} k_2\right) \\ k_4 &= \mathbf{f}_i(U_i^n + \Delta t_n k_3) \end{aligned} \quad (3.33)$$

based on the available approximation at the prior time n .

0				
$\frac{1}{2}$	$\frac{1}{2}$			
$\frac{1}{2}$	0	$\frac{1}{2}$		
1	0	0	1	
	$\frac{1}{6}$	$\frac{1}{3}$	$\frac{1}{3}$	$\frac{2}{6}$

Figure 3.4: Butcher tableaus for the 4th order Runge Kutta time stepping method

To maintain stability of the partial differential equations solved in this discretization, the value of the time step Δt is controlled using methods found in the work done by the Ph.D. dissertation from Müller [2014], who references Cockburn and Shu [1998] and Gassner et al. [2008]. A temporal discretization scheme is defined as stable, “when the solution error is bounded in the whole problem domain for all time steps” (pg. 191 - Schäfer [2006]). Here, the Courant-Friedrichs-Levy criterion c_{CFL} , is used in conjunction with hyperbolic $\Delta t_{n,\alpha}$ and parabolic $\Delta t_{n,\beta}$ time step limiters,

$$\Delta t = \min(\Delta t_{n,\alpha}, \Delta t_{n,\beta}) * c_{CFL}, \quad x \in \Omega_h, \quad (3.34)$$

to maintain stability. The hyperbolic limiter controls the time step found using the time and conservative flux PDEs of the Navier-Stokes equations (1st and 2nd), while the parabolic uses the time and viscous flux PDEs (1st and 3rd). These terms are defined as α and β ,

$$\begin{aligned} \alpha &:= \frac{\alpha^*}{2P+1}, \Delta t_{n,\alpha} = \alpha \frac{h}{\|\underline{u}\| + \sqrt{2}a} \propto \text{Hyperbolic restriction} \\ \beta &:= \frac{\beta^*}{(2P+1)^2}, \Delta t_{n,\beta} = \beta \frac{h^2}{\max\left(\frac{4\mu}{3\rho}, \frac{\mu\mathcal{K}}{\rho Pr}\right)} \propto \text{Parabolic restriction} \end{aligned} \quad (3.35)$$

where α^* and β^* predetermined coefficients, h is the smallest element size in the mesh, \underline{u} is the maximum velocity, and a is the speed of sound. α^* and β^* are chosen by means of experimental results found in the work of Gassner et al. [2008], and can be found in the appendix (A.1).

4 Simulation properties

As with any simulation or experiment, there are many variables that can be adjusted to produce different results in BoSSS. The goal here is to see how these variables need to be adjusted such that the most accurate result can be produced. One important variable already defined in equation (2.10) is the Reynolds number, whose value defines whether a fluid flow is laminar or turbulent, as mentioned by Anderson [2001]. The simulations here are conducted for the laminar flows found at Reynolds numbers 20, 40, 100 and 200. These values are chosen because they are used in many experiments and simulations conducted previously in the field, for which provide a vast amount of baseline data used in this validation. This data is given in the form of dimensionless measurements at values that define laminar fluid flow behavior in both steady and unsteady flow regimes.

4.1 Dimensionless values

The dimensionless values produced in the experimental and numerical data need to be defined in conjunction with the values given in section 2.2, so that they can be compared to the values obtained from the prior experimental and numerical data. These values are defined clearly by Anderson [2001].

For two dimensional flows, the dynamic pressure of the fluid is given by

$$q_\infty = \frac{1}{2} \rho_\infty V_\infty^2. \quad (4.1)$$

This value is used for the coefficients of drag

$$C_D = \frac{d}{q_\infty L_\infty} \quad (4.2)$$

and lift

$$C_L = \frac{l}{q_\infty L_\infty} \quad (4.3)$$

where L_∞ is the characteristic length, i.e. the cylinder diameter $L_\infty = 1$. The values ρ_∞ and V_∞ are set equal to one in accordance to the Dirichlet boundary conditions, which are defined by Schäfer [2006] as boundary condition values that are prescribed before the simulation. d and l are the drag and lift forces, that are each solved numerically in the simulation. These boundary conditions are placed on the mesh, and will be examined more thoroughly in section 4.3. Since all of these dimensionless values are equal to one, the assumption can be made that,

$$C_D = 2 * d \text{ and } C_L = 2 * l. \quad (4.4)$$

The Mach number is defined as

$$M = \frac{V_\infty}{a_\infty}, \quad (4.5)$$

where a_∞ is the speed of sound of the fluid. In the publication by Schäfer [2006] it is stated all fluids at $M \leq 0.3$ behave similarly to fluids under incompressible flow assumptions. The simulations run for this validation use $M = 0.2$ so that previous numerical solutions under incompressible conditions can be accurately compared to the simulation results produced by BoSSS.

The Strouhal number is used to characterize unsteady flows

$$St = \frac{f L_\infty}{V_\infty}, \quad (4.6)$$

where f is the vortex shedding frequency, i.e. $St = f$. This frequency can be found by examining the oscillation of the lift coefficient C_L over time. Doubling the Strouhal number value produces the drag coefficient oscillation frequency f_{CD} .

4.2 Simulation parameters

The simulations carried out for this thesis have various parameters that can be influenced to allow for different solutions. The variables changed are listed as follows:

1. Discontinuous Galerkin order, e.g. DG1, as explained in 3.1.1
2. Element order, e.g. E1, as explained in 3.2
3. Mesh fineness, i.e. the number of elements contained in Ω_h , as explained in 4.3

Another variable to consider is the CFL factor (3.34), which is used in conjunction with the 4th order Runge-Kutta time stepping method. The values of the CFL factor are changed specifically for each simulation to $0 \leq CFL \leq 1$, in order to generate stable time steps that allow for the solution converge. In the publication from Schäffer [2006], it is found that a discretization scheme is convergent when its approximated numerical solution approaches the actual solution. Convergence relies greatly on the stability and consistency of the system, where stability requires the solution error to be bounded in the whole problem domain for all time steps, and consistency requires the discretized equations for $\Delta x, \Delta t \rightarrow 0$ to approach the original differential equations.

In accordance to prior simulations in the field, the element orders used are selected to match the DG orders P of the spatial and viscous discretization. These orders range from 1 to 3, and are written in the notation DG1E1, DG2E2, etc. The number of elements or “fineness” of the Mesh is controlled by a Mesh Parameter MP that only changes the resolution of the grid h , not the size of the different parts of the mesh, e.g. the size of the circle around the cylinder or the height of the wake. The domain size Ω and boundary conditions are also unchanged for different MPs, and remain the same for each grid used as defined in the next section.

4.3 Mesh selection

As described in 3.1.1, the PDEs characterizing the fluid flow are discretized in the spatial domain through use of the DG method. One of the many aspects that make DG and similar high order methods attractive, is their ability to produce accurate results on relatively coarse grids as described by Wang et al. [2012]. For this reason, the meshes used in these simulations do not exceed 5500 elements. There are meshes, however, that are “too-coarse” to run on lower DG orders, and produce inaccurate solutions. These are seen in the simulation results for MP4 meshes.

The grids produced are bound to a 2D domain large enough to accurately represent the effects the cylinder has on the fluid flow, but not so large that the simulations require exhaustive computational effort and time. Depicted on the grid MP4 in figure 4.1 (black lines), the size of the domain for the grids used in these simulations is defined by the variables a , b , and c , and correspond to the values in table 4.1. The values for a , b , and c are picked to be similar to that of the meshes used by Persillon and Braza [1998]. Diagrams for meshes MP 6, 8, and 10 can be found in appendix entries A.2-A.4.

Table 4.1: domain dimensions and number of elements of meshes used

MP	# of elements	a	b	c
4	688	15	30	50
6	1548	15	30	50
8	2752	15	30	50
10	4300	15	30	50

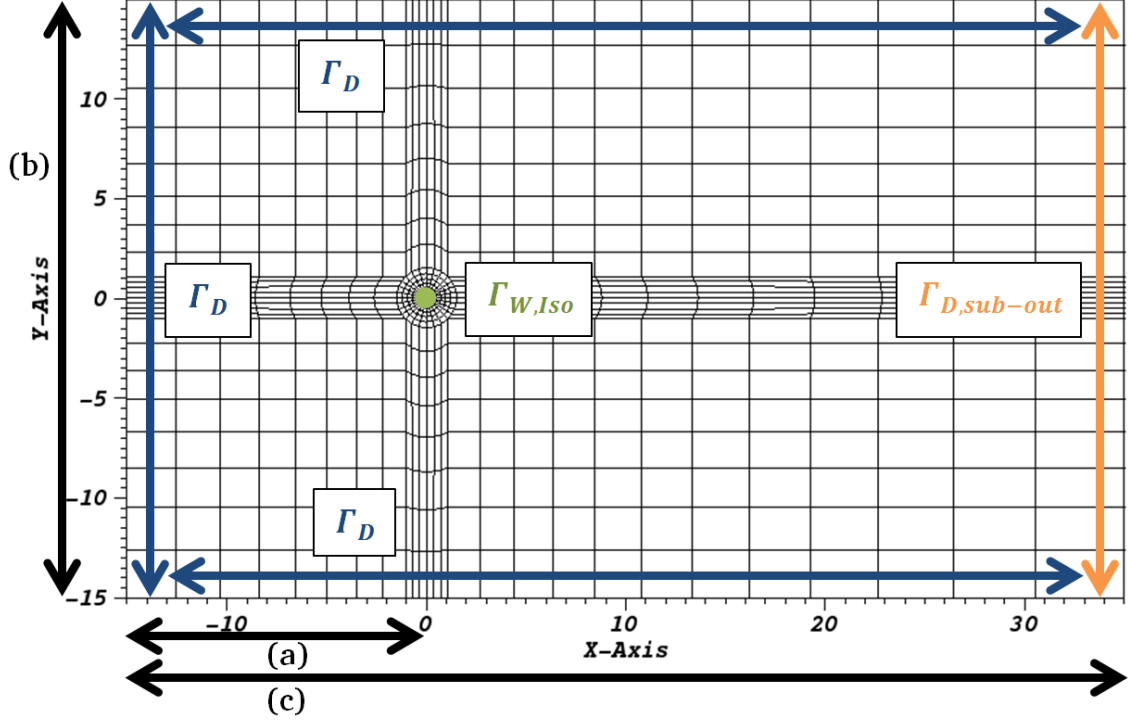


Figure 4.1: domain dimensions and boundary conditions of all meshes depicted on mesh MP4

In order to simulate a horizontal flow towards the cylinder, the Dirichlet freestream initial conditions Γ_D must be applied at the top, bottom, and left boundaries of the grid (seen in blue in figure 4.1). These are, simply, prescribed values given to a flow at $t = 0$ at these boundaries, as seen in the publication by Schäffer [2006]. Here, the velocity in the x-direction u and the density ρ are set equal to one,

$$\Gamma_D : U_{\Gamma_D} = \begin{pmatrix} \rho \\ \rho u \\ 0 \\ 1 \\ \frac{1}{\gamma Ma^2} \end{pmatrix} = \begin{pmatrix} \rho^- \\ \rho u^- \\ \rho v^- \\ \rho E^- \end{pmatrix} = \begin{pmatrix} 1 \\ 1 \\ 0 \\ 17.857 \end{pmatrix}, \quad (4.7)$$

while the energy term is defined in terms of the Mach number, $Ma = 0.2$, and the specific heat ratio for an ideal gas, $\gamma = 1.4$. The values in equation (4.7) that have a (-) represent values outside of the mesh, i.e. initial and boundary conditions (ICs and BCs), while values that have a (+) represent those solved with the DG in the mesh. Seen in orange in figure 4.1, another type of Dirichlet IC called the subsonic outflow BC $\Gamma_{D,sub-out}$ is set at the right side of the domain,

$$\Gamma_{D,sub-out} : U_{\Gamma_{D,sub-out}} = \begin{pmatrix} \rho^+ \\ \rho u^+ \\ \rho v^+ \\ \frac{p^-}{\gamma - 1} + \frac{(\rho u^+)^2 + (\rho v^+)^2}{2\rho^+} \end{pmatrix}. \quad (4.8)$$

This is defined in the work from Hartmann and Houston [2008] and requires a prescribed pressure p^- to be implemented. At the cylinder, the isothermal wall boundary Γ_{wall} (seen in green in figure 4.1) is applied. A wall boundary, as opposed to the Dirichlet boundary, implies zero velocity as defined by Hartmann. The “isothermal” version of this utilizes the Energy term through a prescribed temperature value T_{wall}^-

$$\Gamma_{W-Iso} : U_{\Gamma_{W-Iso}} = \begin{pmatrix} \rho^+ \\ 0 \\ 0 \\ \frac{\rho^+ T_{wall}^-}{\gamma - 1} \end{pmatrix}. \quad (4.9)$$

As found in the energy term for equation (4.7), the prescribed values of T_{wall}^- and p^- for these two conditions are defined as

$$T_{wall}^- = p^- = \frac{1}{\gamma Ma^2} = 17.857. \quad (4.10)$$

It is important to consider wave reflections that might occur at the beginning of the simulation as a result of these boundary conditions. These are mostly seen at the left and right sides of the domain and are often compensated with a larger domain size. For example, in the work by Brehm et al. [2015], a 80Dx80D (D being the diameter of the cylinder) domain is used for simulations. Other options include decreasing a grid’s blockage ratio,

$$\lambda = \frac{D}{b}, \quad (4.11)$$

where the characteristic length L of the cylinder, i.e. its diameter D seen in figure 4.2, is divided by the entire vertical length of the domain. Here, the blockage ratio would be $\lambda = 1/30 = 0.03$, but since the Dirichlet free-stream BCs are implemented, the blockage ratio can be considered to be $\lambda = 0$. This does not, however, completely prevent reflections from occurring, but can be improved with a bigger grid. Since these did not affect the steady state results, no changes to the domain are made.

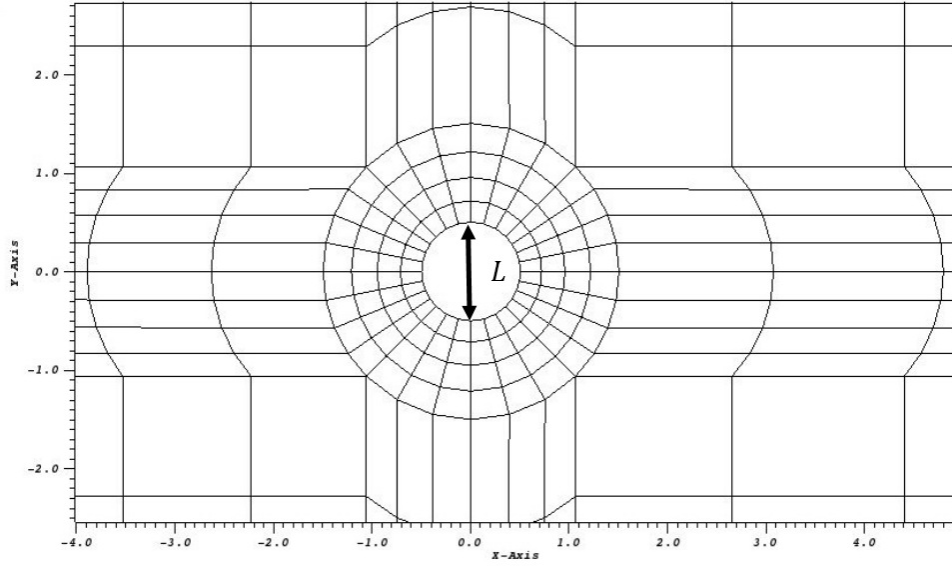


Figure 4.2: close up of the cylinder on the MP4 mesh and its characteristic length L

The degrees of freedom (DOF) of each element of the mesh are also important to consider, when comparing simulation data. These are defined as the number of unknowns being solved within each element of the mesh, and relate directly to the DG order as defined in table 4.2.

Table 4.2: degrees of freedom for each element of a specific DG ordered scheme

DG order	DOF
1	3
2	6
3	10

The total number of degrees of freedom for different simulations is calculated by multiplying the DOF within each element by the total number of elements in the grid, as seen in table 4.3. This is useful because it provides a means of bringing together the discretization method (here DG) and the mesh to be compared with other simulations that use different methods and grids. To test this, the results from the DG3E3MP6 and DG1E1MP11 simulations are compared in the next sections because they have similar total numbers of DOF.

Table 4.3: degrees of freedom for each element of a DG order

DG, E	MP					
	4	6	8	10	11	12
DG1E1	2064	4644	8256	12900	15510	18576
DG2E2	4128	9288	16512	25800	31020	37152
DG3E3	6880	15480	27520	43000	51700	61920

5 Validation of BoSSS for compressible steady flow ($Re \leq 40$)

The following section will list the results acquired during the simulations for steady fluid flow regimes. As mentioned in section 1.1, steady fluid regimes begin at very low Reynolds numbers and end somewhere between $40 < Re < 55$. The values used to define the fluid flow at these regimes are the previously defined coefficient of drag C_D , and the newly introduced length of separation W^* seen in figure 5.1 as defined by Brehm et al. [2015]. This is defined as the “wake length” behind the cylinder’s trailing vortices where the velocity is zero, and is a measurement often used in experiments and simulations previously conducted in the field.

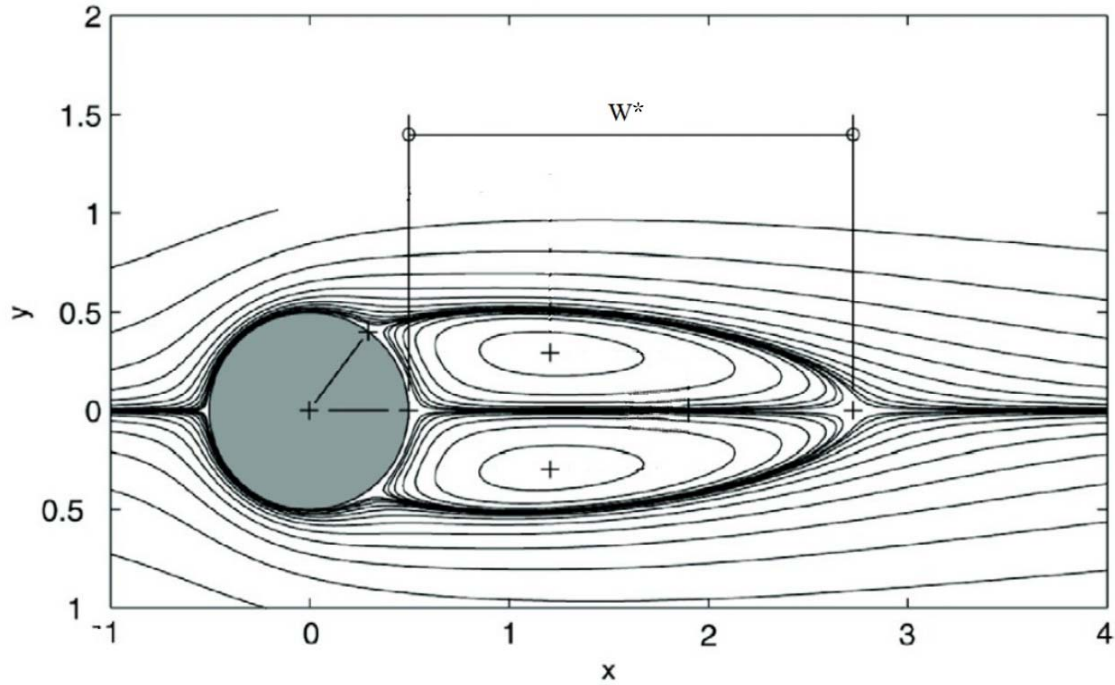


Figure 5.1: cylinder in a steady flow regime with the defined wake separation length W^* , taken from Brehm et al. [2015] (modified)

5.1 Simulation at $Re=20$

The work implemented here will now be compared to the results of experiments and other simulations conducted in the field for $Re = 20$. Table 5.1 shows the methods used by others and their corresponding wake separation lengths and drag coefficients in comparison to the finest simulation run for this validation. The data is in good agreement.

Table 5.1: comparison of previous wake separation lengths and coefficient of drag data with present results for $Re = 20$

$Re = 20$	Source	2D/3D	W^*	C_D
Numerical – Incompressible	Dennis et al. [1970]	2D	0.94	2.05
	Forberg [1980]	2D	0.91	2.00
	Linnick et al. [2005]	2D	0.93	2.06
Experimental	Coutanceau et al. [1978]	-	0.93	-
	Tritton [1959]	-	-	2.09
Numerical – Compressible	Brehm et al. [2015] ($Ma = 0.1$)	3D	0.96	2.02
	Present Results:	2D	0.975	2.06

The simulations ran by Brehm et al. [2015] also solved the compressible Navier-Stokes equations like this validation, but in three dimensions rather than two. Since the Mach number used by Brehm is small like the $Ma = 0.2$ value used in this validation, the flow is considered to be incompressible, and can be accurately compared to the rest of the previous numerical solutions.

The wake separation lengths and coefficients of drag for each simulation are presented in tables 5.1 and 5.2. Here it is made clear that the coarser meshes used at lower DG produce very inaccurate results, e.g. DG1E1MP4 and DG1E1MP6. Also, the simulations that have similar degrees of freedom, DG1E1MP11 and DG3E3MP6, show a more accurate solution in the higher DG order for the wake separation length, and an equally accurate value in the drag coefficients.

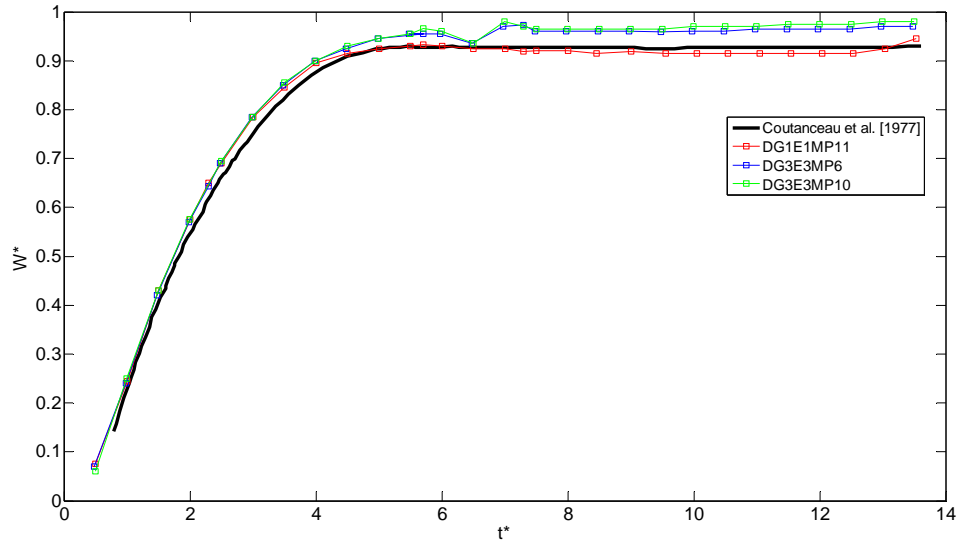
Table 5.2: wake separation lengths for each simulation for $Re = 20$

W^*	MP				
	4	6	8	10	11
DG1E1	0.600	0.810	0.880	0.905	0.920
DG2E2	0.935	0.960	0.950	0.950	-
DG3E3	0.970	0.973	0.975	0.975	-

Table 5.3: coefficients of drag for each simulation for $Re = 20$

C_D	MP				
	4	6	8	10	11
DG1E1	1.989	2.054	2.068	2.075	2.075
DG2E2	2.168	2.149	2.119	2.111	-
DG3E3	2.109	2.078	2.065	2.057	-

The value of the wake separation length over time is depicted graphically in figure 5.2, where simulations DG3E3MP10 (green), DG3E3MP6 (blue), and DG1E1MP11 (red) are compared to the experimental results found by Coutanceau and Bouard [1978]. The presence of a wave reflection from the left side of the domain can be seen at about $t^* = 7$, where the wake length fluctuates slightly. Regardless, the validation results relate to the prior experiments very well as the system reaches its steady state, e.g. $t^* = 14$. This is also represented in the vorticity around the cylinder in figure 5.3. This shows the expected symmetric vortices previously introduced in section 1.1 in figure 1.1.

**Figure 5.2:** wake separation lengths of simulations DG3E3MP6, DG3E3MP10, and DG1E1MP11 in comparison to experiments from Coutanceau and Bouard [1978] for $Re = 20$

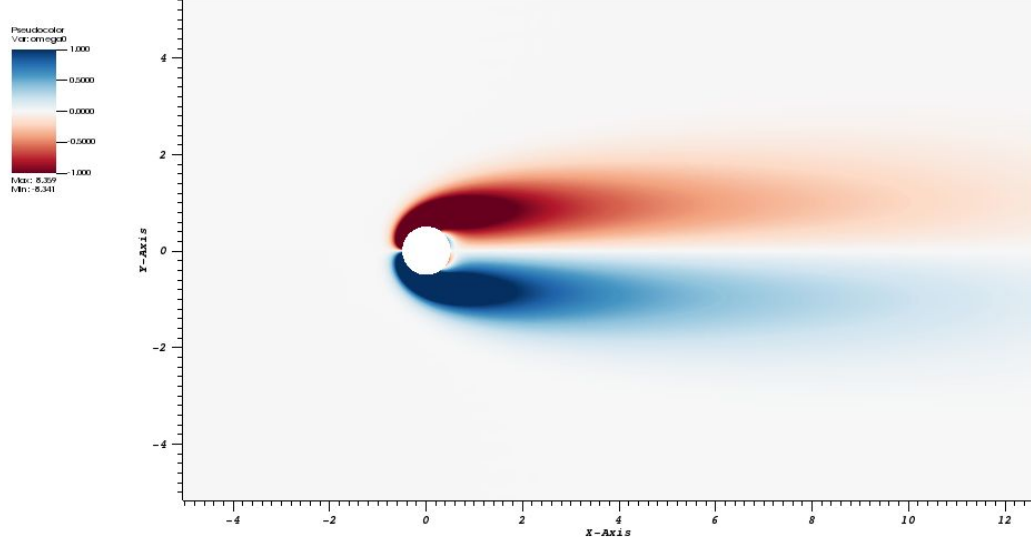


Figure 5.3: the vorticity in the wake of simulation DG3E3MP10 for $Re = 20$

5.2 Simulation at $Re=40$

As for the simulations conducted for $Re = 20$ the values used to validate the simulations at $Re = 40$ are the wake separation length and the coefficient of drag. The finest solution, i.e. the simulation run at the highest DG order on the finest mesh, achieved is compared to various numerical and experimental results conducted in the field in table 5.3. All the values are in good agreement.

Table 5.4: comparison of previous wake separation lengths and coefficient of drag with present results for $Re = 40$

$Re = 40$	Source	2D/3D	W^*	C_D
Numerical – Incompressible	Dennis et al. [1970]	2D	2.35	1.52
	Forberg [1980]	2D	2.24	1.50
	Linnick et al. [2005]	2D	2.28	1.54
Experimental	Coutanceau et al. [1978]	-	2.13	-
	Tritton [1959]	-	-	1.59
Numerical – Compressible	Brehm et al. [2015] ($M = 0.1$)	3D	2.26	1.51
	Present Results:	2D	2.250	1.605

Only the DG3E3MP10, DG3E3MP6, and DG1E1MP11 simulations are conducted for $Re = 40$ because of the high level of accuracy achieved for steady fluid flows in the $Re = 20$ results. The values of each simulation are depicted in table 5.4. Also, the simulations that have similar degrees of freedom, DG1E1MP11 and DG3E3MP6, show a more accurate solution for the coarser mesh at higher DG order for both the wake separation length and the drag coefficient.

Table 5.5: wake separation lengths and coefficients of drag for each simulation for $Re = 40$

Simulation	W^*	C_D
DG1E1MP11	2.19	1.50
DG3E3MP6	2.27	1.60
DG3E3MP10	2.25	1.61

The values for the wake separation length as a function of time are depicted graphically in figure 5.4, where the simulations are compared again to the experimental results found in the work by Coutanceau and Bouard [1978] for $Re = 40$. The wave reflection here, though difficult to see in the graph, occurs earlier than that of the $Re = 20$ simulations at around $t^* = 6$. These validation results correlate very well to the prior experiments, and show that the higher order simulations are slightly more accurate than that of the DG1E1MP11 simulation. The vorticity of the DG3E3MP10 simulation is depicted in figure 5.5, showing slightly longer vortices in the wake than those in the $Re = 20$ simulations.

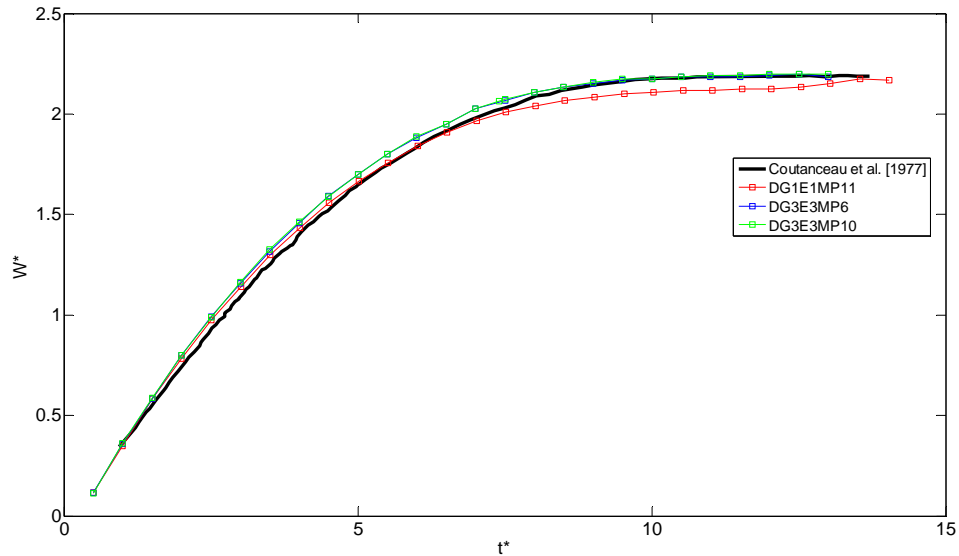


Figure 5.4: wake separation lengths of simulations DG3E3MP6, DG3E3MP10, and DG1E1MP11 in comparison to experiments from Coutanceau and Bouard [1978] for $Re = 40$

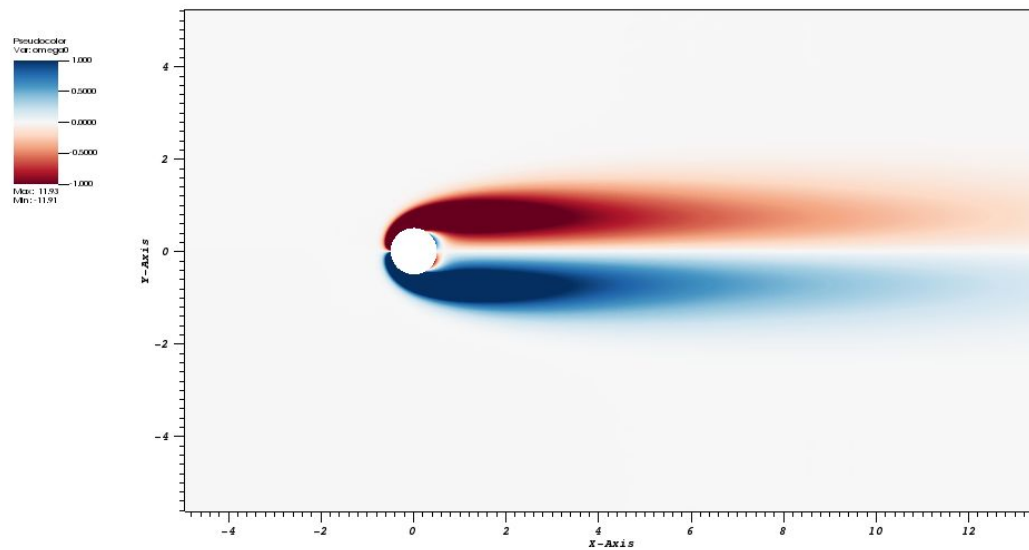


Figure 5.5: the vorticity in the wake of simulation DG3E3MP10 for $Re = 40$

6 Validation of BoSSS for unsteady flow ($Re > 40$)

The following section contains the results from the simulations conducted for unsteady fluid flow. Cited previously in section 4.2 in the work by Anderson [2001], the values used to define the fluid flow at these regimes are the coefficient of lift C_L , the coefficient of drag C_D , and the Strouhal number St , which is used explicitly for unsteady fluid flows in its use of the vortex shedding frequency f (4.6). Like the results from the steady regimes, these values are found in various simulations for $Re = 100$ and $Re = 200$, and compared with results from experiments and other numerical simulations.

As mentioned in section 1.1, the unsteady fluid regime for laminar flows begins somewhere between $40 < Re < 55$, but require a perturbation to initiate vortex shedding in the wake of the cylinder. A perturbation can be anything that causes a disturbance in the flow, like an initial vortex, or a shift in the location of the cylinder. Here the former was used, and is depicted in figure 6.1 at $t = 0$ of a simulation, where the red and blue colors each represent negative and positive vortices, respectively.

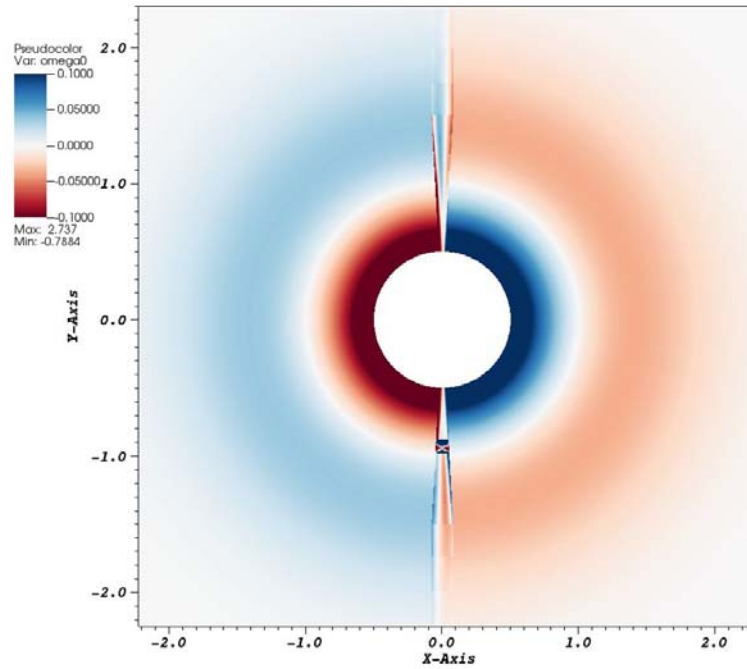


Figure 6.1: the initial perturbation used to catalyze vortex shedding for simulations at $Re = 100$ and 200

Another aspect of unsteady fluid flow is the possible onset of 3D disturbances in wake at $Re = 180$, as found in the work from Williamson [1989], and referenced by vich [1996]. This value has been the subject of much debate, as mentioned in section 1.1, and will not be explored in this thesis since these simulations are only run in 2D.

6.1 Simulation at $Re=100$

The work implemented here will now be compared to the results of experiments and other simulations conducted in the field for $Re = 100$. Table 6.1 shows the methods used by others and their corresponding values in comparison to the finest simulation achieved for this validation. The data is in good agreement.

Table 6.1: comparison of previous Strouhal numbers, and coefficients of drag and lift with present validation results for $Re = 100$

$Re = 100$	Source	2D/3D	St	C_D	C_L
Numerical – Incompressible	Gresho et al. [1984]	2D	0.18	1.76	-
	Linnick et al. [2005] ($\lambda = 0.056$)	2D	0.169	1.38 ± 0.010	± 0.337
	Linnick et al. [2005] ($\lambda = 0.023$)	2D	0.166	1.34 ± 0.009	± 0.333
	Persillon et al. [1998]	2D	0.165	1.253	-
	Saiki et al. [1996]	2D	0.171	1.26	-
	Persillon et al. [1998]	3D	0.164	1.240	-
	Liu et al. [1998]	3D	0.165	1.35 ± 0.012	± 0.339
Experimental	Berger et al. [1972]	-	0.16-0.17	-	-
	Clift et al. [1978]	-	-	1.24	-
	Williamson[1996]	-	0.164	-	-
Numerical – Compressible	Brehm et al. [2015] ($M = 0.1$)	3D	0.165	1.32 ± 0.01	± 0.32
	Present Results	2D	0.167	1.371 ± 0.011	± 0.333

The finest solution is from the simulation that was run on the finest mesh at the highest DG order, i.e. DG3E3MP10. The values for this simulation with respect to time are depicted in figures 6.2, where the Strouhal number is taken to be the frequency of the oscillating lift coefficient C_L (figure 6.2a), and the drag coefficient C_D oscillates at double this value (figure 6.2b). Shown in figures 6.2c and 6.2d, the initial vortex perturbation can be seen at the very beginning of the simulation where these values suddenly increase before quickly dissipating. Also, it is clear to see that the simulation does not reach a steady state solution until about $t = 70s$.

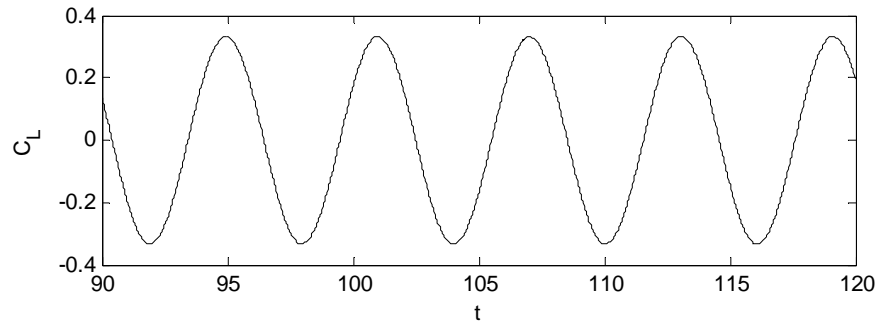


Figure 6.2a: the value of the lift coefficient over for $90 < t < 120$ for simulation DG3E3MP10 at $Re = 100$

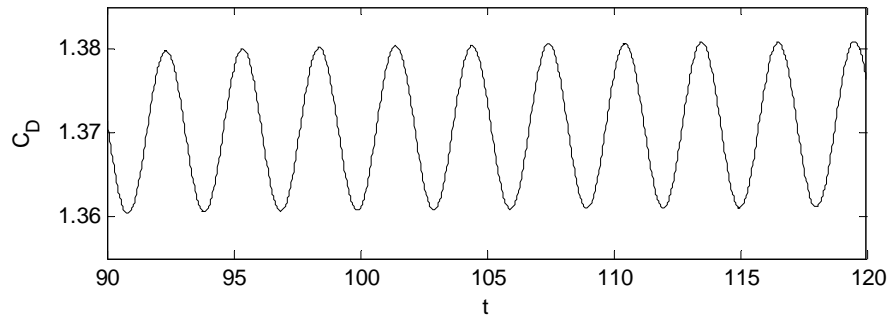


Figure 6.2b: the value of the drag coefficient over for $90 < t < 120$ for simulation DG3E3MP10 at $Re = 100$

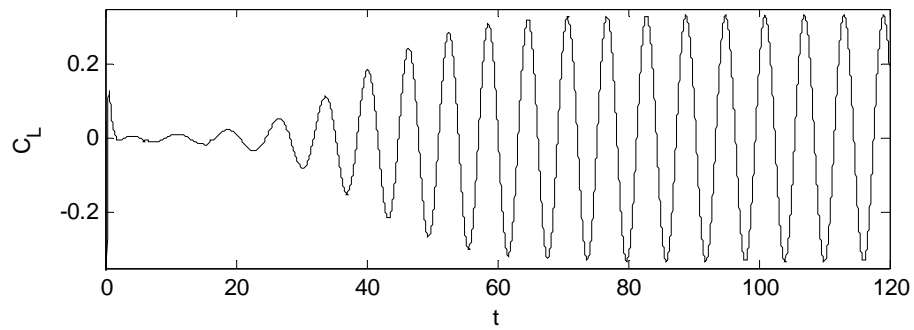


Figure 6.2c: the value of the lift coefficient over for $0 < t < 120$ for simulation DG3E3MP10 at $Re = 100$

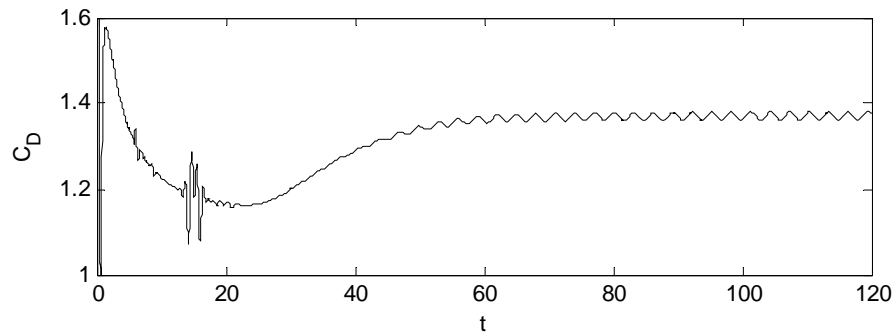


Figure 6.2d: the value of the drag coefficient over for $0 < t < 120$ for simulation DG3E3MP10 at $Re = 100$

A spatial representation of the von Kármán vortex street introduced in section 1 can be seen in figure 6.3 for the DG3E3MP10 simulation. When measured, it can be seen that the vortices oscillate at the same frequency of the lift coefficient, which is the value used to define the Strouhal number.

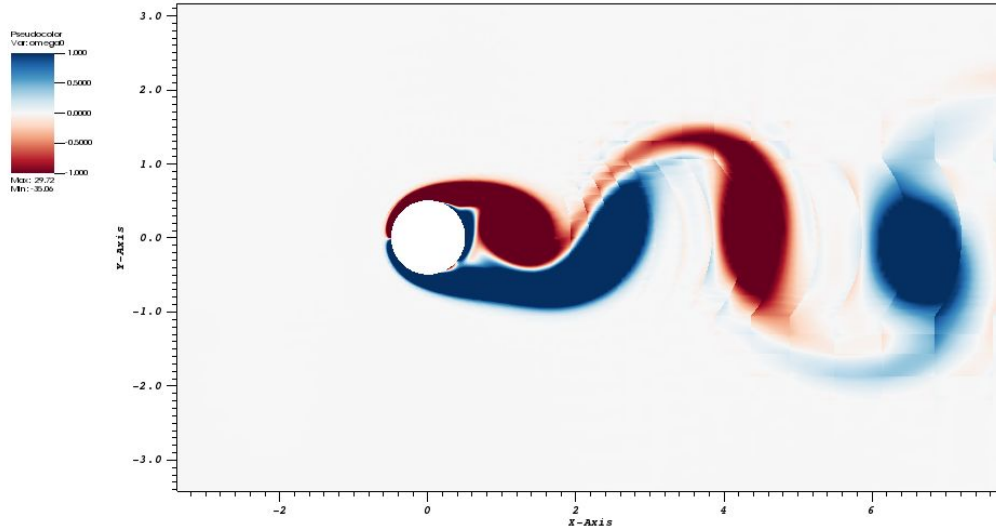


Figure 6.3: the vorticity in the wake of simulation DG3E3MP10 for $Re = 100$

These same resulting values are shown below in tables 6.3, 6.4, and 6.5 for each simulation. Here the average values of the lift and drag coefficients are given with a plus-minus sign to show the amplitude of their oscillation. The two simulations with similar total numbers of DOF yield similar results for the Strouhal number and lift coefficient, but show that the higher order simulation (DG3E3MP10) is slightly more accurate than the lower order simulation (DG1E1MP11) for the drag coefficient.

Table 6.2: the values for the Strouhal number for all simulations at $Re = 100$

St	MP				
	4	6	8	10	11
DG1E1	0.101	0.135	0.168	0.167	0.167
DG2E2	0.134	0.167	0.168	0.167	-
DG3E3	0.168	0.167	0.167	0.167	-

Table 6.3: the values for the lift coefficient for all simulations at $Re = 100$

C_L	MP				
	4	6	8	10	11
DG1E1	± 0.001	± 0.221	± 0.283	± 0.298	± 0.303
DG2E2	± 0.382	± 0.313	± 0.322	± 0.328	-
DG3E3	± 0.362	± 0.331	± 0.333	± 0.333	-

Table 6.4: the values of the drag coefficient for all simulations at $Re = 100$

C_D	MP				
	4	6	8	10	11
DG1E1	0.955 ± 0.001	1.199 ± 0.009	1.264 ± 0.007	1.279 ± 0.008	1.284 ± 0.008
DG2E2	1.368 ± 0.015	1.365 ± 0.010	1.373 ± 0.009	1.373 ± 0.010	-
DG3E3	1.390 ± 0.014	1.377 ± 0.011	1.373 ± 0.011	1.371 ± 0.011	-

The values in table 6.4 are represented graphically for DG1E1 (red), DG2E2 (blue), and DG3E3 (green), where the coefficient of drag is a function of the fineness of the mesh (MP). This helps solidify the idea that higher DG order produces more accurate solutions for coarser meshes, e.g. DG2E2MP4, DG3E3MP6, etc., than lower DG orders for finer meshes.

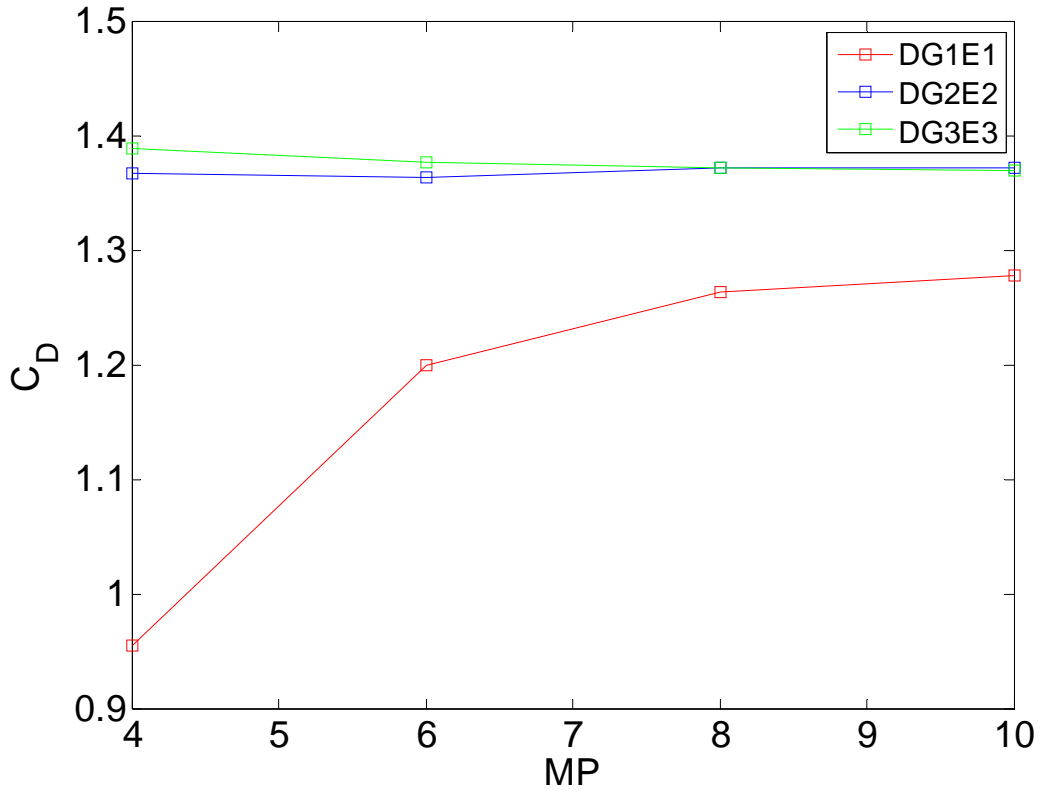


Figure 6.4: graphical representation of table 6.4 for the drag coefficient as a function of the MP for $Re = 100$

6.2 Simulation at $Re=200$

As was done for $Re = 100$, the results from the simulations implemented here will now be compared to the results of experiments and other simulations conducted in the field for $Re = 200$. Table 6.5 shows the methods used by others and their corresponding values in comparison to the finest simulation achieved for this validation. The data correlates well to the previous data.

it can be seen, however, that the present results match fairly well to the data for the other 2D numerical simulations, but show a higher value than the data for the 3D numerical and experimental results. This could be a result of possible 3D disturbances in the wake that are not represented in the 2D flow.

Table 6.5: comparison of previous Strouhal numbers, and coefficients of drag and lift with present validation results for $Re = 200$

$Re = 200$ Analysis type	Source	2D/3D	St	C_D	C_L
Numerical – Incompressible	Belov et al. [1995]	2D	0.193	1.19 ± 0.042	± 0.64
	Gresho et al. [1984]	2D	0.21	1.76	-
	Linnick et al. [2005] ($\lambda = 0.056$)	2D	0.199	$1.37 \pm 0.046 \sim$	± 0.70
	Linnick et al. [2005] ($\lambda = 0.023$)	2D	0.197	1.34 ± 0.044	± 0.69
	Miyake et al. [1992]	2D	0.196	1.34 ± 0.043	± 0.67
	Persillon et al. [1998]	2D	0.198	1.321	-
	Saiki et al. [1996]	2D	0.197	1.18	-
	Persillon et al. [1998]	3D	0.181	1.306	-
	Liu et al. [1998]	3D	0.192	1.31 ± 0.049	± 0.69
Experimental	Berger et al. [1972]	-	0.18-0.19	-	-
	Clift et al. [1978]	-	-	1.16	-
	Williamson [1996]	-	0.181 \sim	-	-
Numerical – Compressible	Brehm et al. [2015]	3D	0.192	1.3 ± 0.04	± 0.66
	Present Results	2D	0.201	1.371 ± 0.011	± 0.70

(\sim) Approximate value.

As was done for the $Re = 100$ simulations, the values for the lift and drag coefficients for the $Re = 200$, DG3E3MP10 simulation are depicted in figures 6.5 with respect to time. The Strouhal number can be found by finding the frequency of the lift coefficient, which shows that the vortices oscillate faster than the simulations at $Re = 100$. These vortices are represented spatially in figure 6.6. Additionally, it can be seen in figures 6.5c and 6.5d that the steady state solution is reached at about $t = 50s$, which is 20 seconds earlier than the $Re = 100$ results.

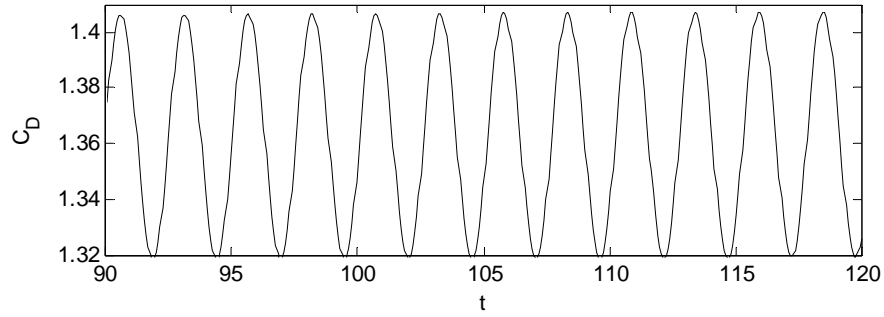


Figure 6.5a: the value of the coefficient of drag over for $90 < t < 120$ for simulation DG3E3MP10 at $Re = 200$

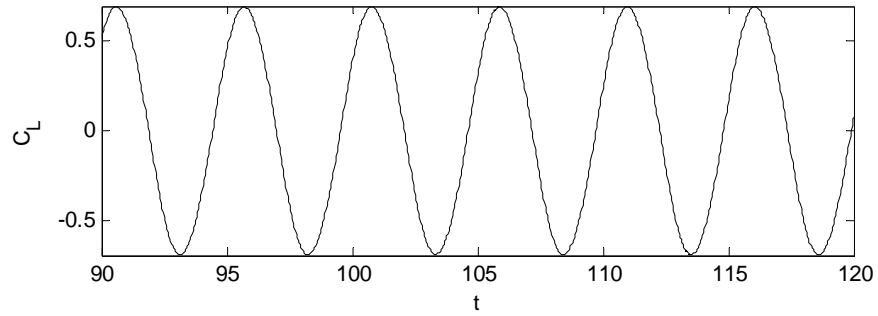


Figure 6.5b: the value of the coefficient of lift over for $90 < t < 120$ for simulation DG3E3MP10 at $Re = 200$

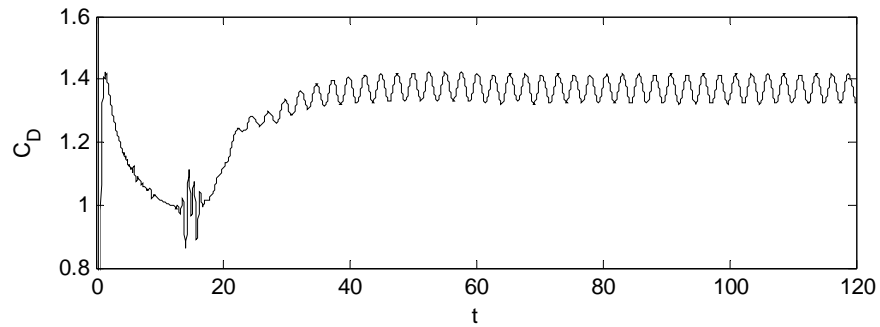


Figure 6.5c: the value of the coefficient of drag over for $0 < t < 120$ for simulation DG3E3MP10 at $Re = 200$

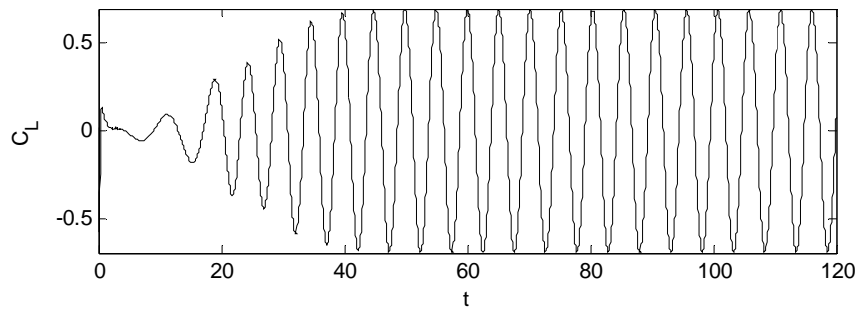


Figure 6.5d: the value of the coefficient of lift over for $0 < t < 120$ for simulation DG3E3MP10 at $Re = 200$

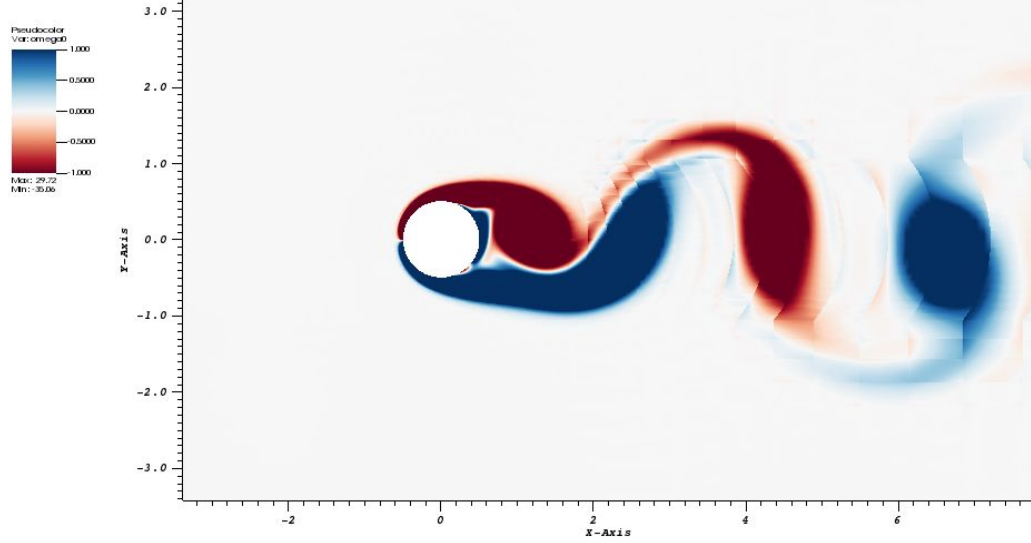


Figure 6.6: the vorticity in the wake of simulation DG3E3MP10 for $Re = 200$

The values for the Strouhal number, lift coefficient, and drag coefficient are depicted in tables 6.6, 6.7, and 6.8 for each simulation. The two simulations with similar total numbers of DOF yield accurate, similar results for the Strouhal number, but show that the drag and lift coefficients for the higher order simulation (DG3E3MP10) are slightly more accurate those of lower order simulation (DG1E1MP11).

Table 6.6: the values for the Strouhal number for all simulations at $Re = 200$

St	MP				
	4	6	8	10	11
DG1E1	0.101	0.169	0.167	0.201	0.201
DG2E2	0.168	0.201	0.201	0.201	0
DG3E3	0.201	0.201	0.201	0.201	0

Table 6.7: the values for the lift coefficient for all simulations at $Re = 200$

C_L	MP				
	4	6	8	10	11
DG1E1	± 0.015	± 0.464	± 0.595	± 0.609	± 0.614
DG2E2	± 0.746	± 0.676	± 0.654	± 0.677	-
DG3E3	± 0.657	± 0.7	± 0.696	± 0.696	-

Table 6.8: the values for the drag coefficient for all simulations at $Re = 200$

C_D	MP				
	4	6	8	10	11
DG1E1	0.713 ± 0.001	1.174 ± 0.02	$1.2930.031$	1.294 ± 0.013	1.292 ± 0.034
DG2E2	1.434 ± 0.045	1.339 ± 0.044	1.345 ± 0.043	1.364 ± 0.045	-
DG3E3	1.37 ± 0.045	1.382 ± 0.048	1.375 ± 0.049	1.371 ± 0.049	-

The values in table 6.8 are represented graphically for DG1E1 (red), DG2E2 (blue), and DG3E3 (green), where the coefficient of drag is a function of mesh parameter. Like for $Re = 100$, this helps visually depict the difference in accuracy between simulations at higher DG order on coarser meshes and simulations at lower DG order on finer meshes.

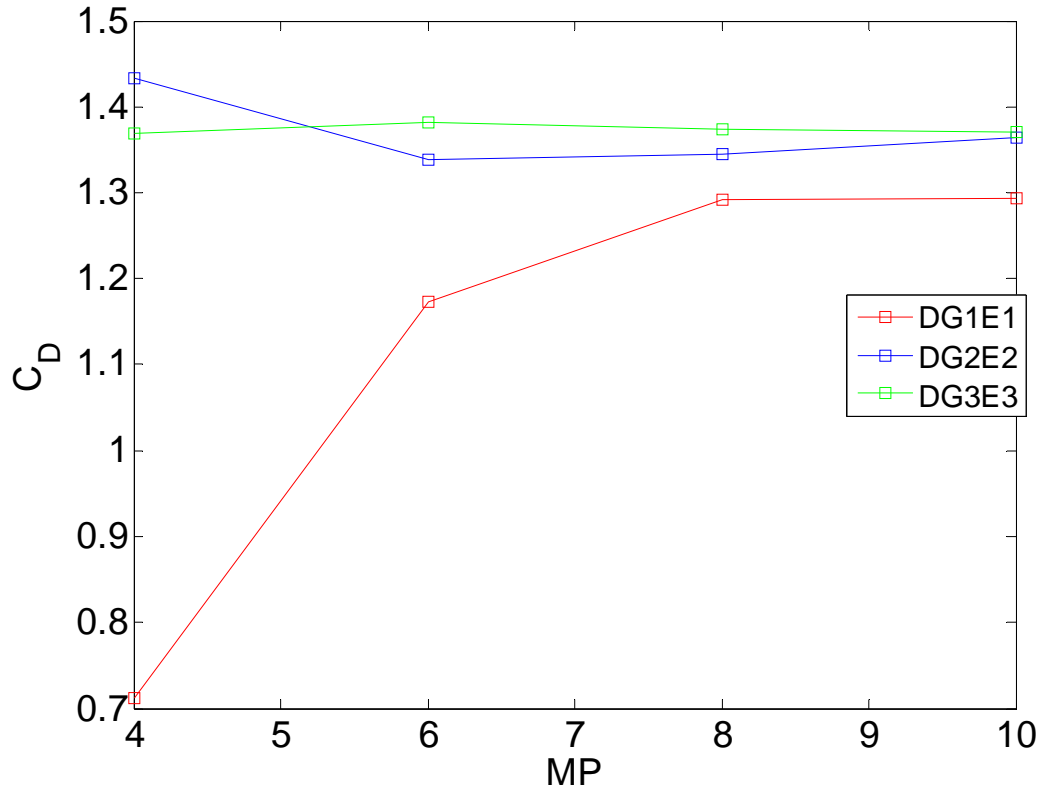


Figure 6.7: graphical representation of table 6.8 for the drag coefficient as a function of the MP for $Re = 200$

7 Conclusion

This bachelor thesis successfully validates the CNS extension of BoSSS for both steady and unsteady fluid flows in two dimensions. The results obtained by the simulations at Reynolds numbers 20, 40, 100, and 200 match closely to those of previous simulations and experiments in the field. The results from simulations at 2nd and 3rd DG orders produce such precise and accurate values that the exploration of using higher DG orders seems unnecessary.

Though simulations with similar total numbers of DOF are theorized to have about the same computational effort, these simulations show that the results at higher DG orders on coarser meshes produce equal to better results than those at lower DG orders on finer meshes. This allows for less time spent on mesh generation.

There was an extensive effort, however, devoted to finding the best domain size and number of elements for the grids used for these simulations. It became evidently clear that the domain must be large enough to help prevent wave reflections while allowing for accurate results in the wake, but not so large that the simulation requires exhaustive computational effort. In the future, the use of different boundary conditions should be explored to help prevent these reflections.

Also, as mentioned by Utz [2014], the use of mixed order grids, i.e. elements in a grid have different curvature, should be explored to help improve the performance of calculations. The idea here is to make boundary edges curved while keeping the internal edges linear.

In the next step, it would be beneficial to conduct simulations for both $Re = 100$ and $Re = 200$ in 3D to find the degree at which the 3D disturbances are affecting the solutions. Like that of the work by Persillon and Braza [1998], these results could be compared to the 2D simulations. This would better prove the accuracy of the CNS extension.

Beyond that, the next step would be to explore the accuracy of the CNS extension for turbulent flows. With this, the possibility to run the extension at higher DG orders, e.g. 4th or 5th order, remains available.

8 Appendix

Figure A.1: predetermined coefficients α^* and β^* used in the temporal discretization, taken from Gassner et al. [2008]

Figure A.2: mesh MP6

Figure A.3: mesh MP8

Figure A.4: mesh MP10

p	1	2	3	4	5
α^*	1.3	1.1	0.9	0.7	0.7
β^*	1.5	0.7	0.35	0.25	0.13

Figure A.1: predetermined coefficients α^* and β^* used in the temporal discretization, taken from Gassner et al. [2008]

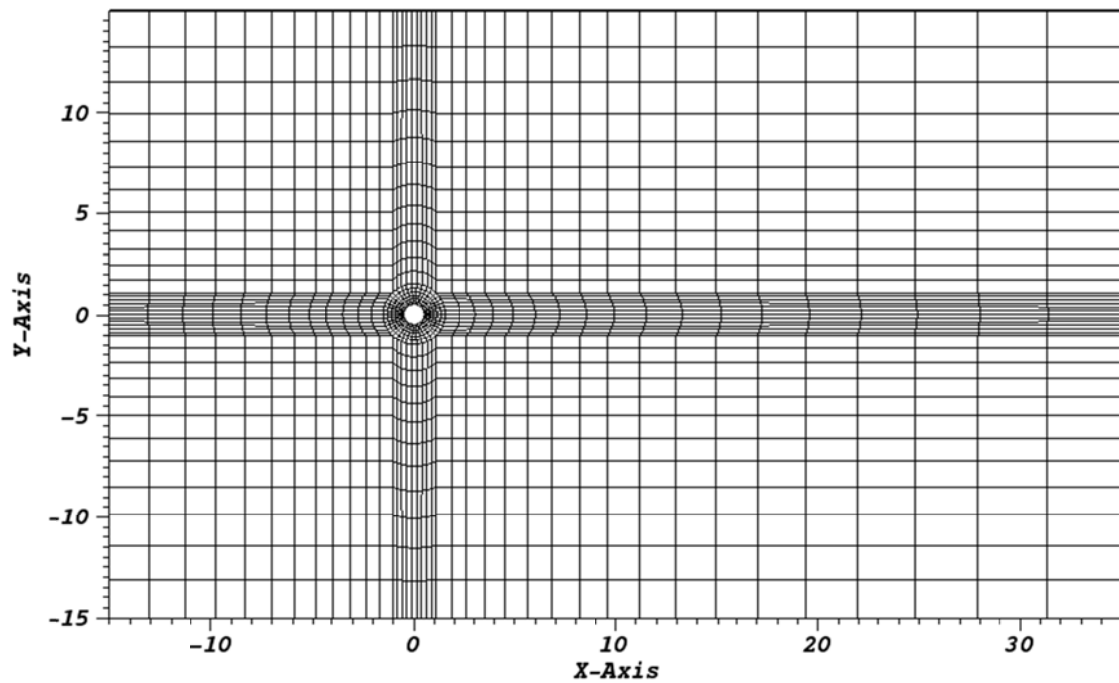


Figure A.2: mesh MP6

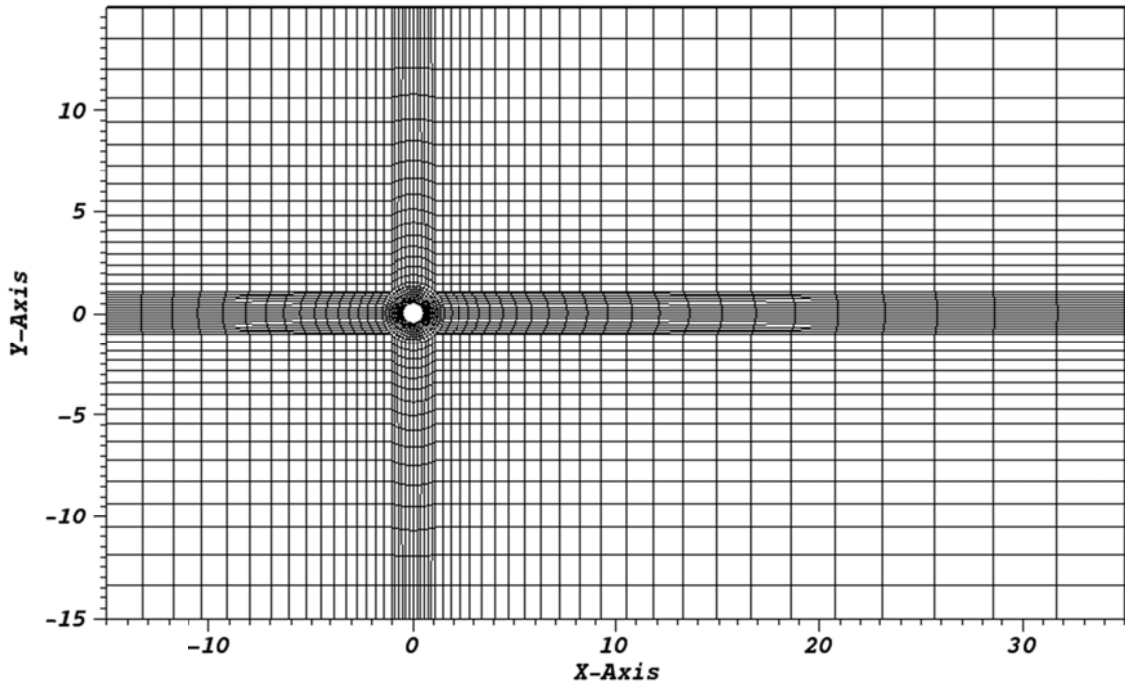


Figure A.3: mesh MP8

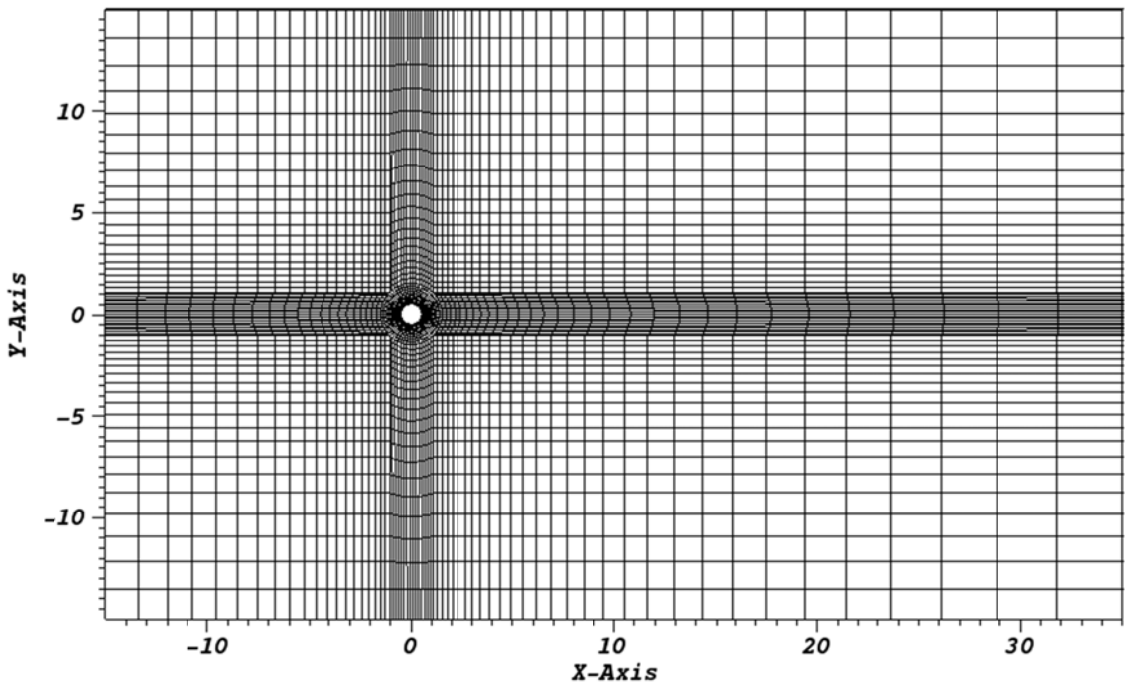


Figure A.4: mesh MP10

List of Figures

1.1	Steady and unsteady wakes behind a circular cylinder, taken from Williamson [1996]	2
3.1	1D element discretization of elements \mathcal{K}_{i-1} , \mathcal{K}_{i-1} , and \mathcal{K}_i with corresponding edges.....	6
3.2	The transformation T_l used from the reference element $\hat{\mathcal{K}}$ to \mathcal{K}_l in the computational domain for a third order element, taken from Utz [2014].....	10
3.3	Three different possible transformations for linear, bilinear, and quadratic elements, where the top contain the elements in the reference domain and the bottom contains the elements in the Cartesian domain, taken from Utz [2014].....	11
3.4	Butcher tableaus for the 4th order Runge Kutta time stepping method.....	13
4.1	Domain dimensions and boundary conditions of all meshes depicted on mesh MP4.....	16
4.2	Close up of the cylinder on the MP4 mesh and its characteristic length L	18
5.1	Cylinder in a steady flow regime with the defined wake separation length W^* , taken from Brehm et al. [2015] (modified).....	19
5.2	Wake separation lengths of simulations DG3E3MP6, DG3E3MP10, and DG1E1MP11 in comparison to experiments from Coutanceau and Bouard [1978] for $Re = 20$	21
5.3	The vorticity in the wake of simulation DG3E3MP10 for $Re = 20$	22
5.4	Wake separation lengths of simulations DG3E3MP6, DG3E3MP10, and DG1E1MP11 in comparison to experiments from Coutanceau and Bouard [1978] for $Re = 40$	23
5.5	The vorticity in the wake of simulation DG3E3MP10 for $Re = 40$	24
6.1	The initial perturbation used to catalyze vortex shedding for simulations at $Re = 100$ and 200	25
6.2	a, b, c, and d: the lift and drag coefficients with respect to time for $Re = 100$	27
6.3	The vorticity in the wake of simulation DG3E3MP10 for $Re = 100$	28
6.4	Graphical representation of table 6.4 for the drag coefficient as a function of the MP for $Re = 100$	29
6.5	a, b, c, and d: the lift and drag coefficients with respect to time for $Re = 200$	31
6.6	The vorticity in the wake of simulation DG3E3MP10 for $Re = 200$	32
6.7	Graphical representation of table 6.8 for the drag coefficient as a function of the MP for $Re = 200$	33

List of Tables

4.1	Domain dimensions and number of elements of meshes used.....	16
4.2	Degrees of freedom for each element of a specific DG ordered scheme.....	18
4.3	Degrees of freedom for each element of a DG order.....	18
5.1	Comparison of previous wake separation lengths and coefficient of drag data with present results for $Re = 20$	20
5.2	Wake separation lengths for each simulation for $Re = 20$	20
5.3	Coefficients of drag for each simulation for $Re = 20$	21
5.4	Comparison of previous wake separation lengths and coefficient of drag with present results for $Re = 40$	22
5.5	Wake separation lengths and coefficients of drag for each simulation for $Re = 40$	23
6.1	Comparison of previous Strouhal numbers, and coefficients of drag and lift with present validation results for $Re = 100$	26
6.2	The values for the Strouhal number for all simulations at $Re = 100$	28
6.3	The values for the lift coefficient for all simulations at $Re = 100$	28
6.4	The values of the drag coefficient for all simulations at $Re = 100$	29
6.5	Comparison of previous Strouhal numbers, and coefficients of drag and lift with present validation results for $Re = 200$	30
6.6	The values for the Strouhal number for all simulations at $Re = 200$	32
6.7	The values for the lift coefficient for all simulations at $Re = 200$	32
6.8	The values for the drag coefficient for all simulations at $Re = 200$	33

Bibliography

- A. Belov, L. Martinelli, A. Jameson, A. Belov, L. Martinelli, and A. Jameson, “A new implicit algorithm with multigrid for unsteady incompressible flow calculations,” *AIAA 4 PAPER 9510049, AIAA 33RD AEROSPACE SCIENCES MEETING*, 1995.
- Bengt Fornberg, “A numerical study of steady viscous flow past a circular cylinder,” (English), *Journal of Fluid Mechanics*, vol. 98, no. 04, pp. 819–855, 1980.
- E. Berger and R. Wille, “Periodic Flow Phenomena,” (en), *Annual Review of Fluid Mechanics*, vol. 4, pp. 313–340, 1972.
- Björn Müller, “Methods for higher order numerical simulations of complex inviscid fluids with immersed boundaries,” PhD, Fachbereich Maschinenbau, Technische Universität Darmstadt, Darmstadt, 2014.
- L. Botti, “Influence of Reference-to-Physical Frame Mappings on Approximation Properties of Discontinuous Piecewise Polynomial Spaces: Journal of Scientific Computing,” (English), *J Sci Comput*, vol. 52, no. 3, pp. 675–703, 2012.
- C. Brehm, C. Hader, and H. F. Fasel, “A locally stabilized immersed boundary method for the compressible Navier–Stokes equations,” *Journal of Computational Physics*, vol. 295, pp. 475–504, 2015.
- R. Clift, J. R. Grace, and M. E. Weber, *Bubbles, drops, and particles*. New York: Academic Press, 1978.
- B. Cockburn and C.-W. Shu, “The Runge–Kutta Discontinuous Galerkin Method for Conservation Laws V: Multidimensional Systems,” *Journal of Computational Physics*, vol. 141, no. 2, pp. 199–224, 1998.
- M. Feistauer, J. Felcman, and I. Straškraba, *Mathematical and computational methods for compressible flow*: Oxford University Press, 2003.
- G. Gassner, F. Lörcher, and C.-D. Munz, “A discontinuous Galerkin scheme based on a space-time expansion II. Viscous flow equations in multi dimensions,” *Journal of Scientific Computing*, vol. 34, no. 3, pp. 260–286, 2008.
- P. M. Gresho, S. T. Chan, R. L. Lee, and C. D. Upson, “A modified finite element method for solving the time-dependent, incompressible Navier–Stokes equations. Part 2: Applications,” *International Journal for Numerical Methods in Fluids*, vol. 4, 1984.
- R. Hartmann and P. Houston, “Adaptive Discontinuous Galerkin Finite Element Methods for the Compressible Euler Equations,” *Journal of Computational Physics*, vol. 183, no. 2, pp. 508–532, 2002.
- R. Hartmann and P. Houston, “An optimal order interior penalty discontinuous Galerkin discretization of the compressible Navier–Stokes equations,” *Journal of Computational Physics*, vol. 227, no. 22, pp. 9670–9685, 2008.
- HÉLÈNE PERSILLON and MARIANNA BRAZA, “Physical analysis of the transition to turbulence in the wake of a circular cylinder by three-dimensional Navier–Stokes simulation,” (English), *Journal of Fluid Mechanics*, vol. 365, pp. 23–88, 1998.

-
- J. S. Hesthaven and T. Warburton, “Nodal discontinuous Galerkin methods: Algorithms, analysis and applications,” 2008.
- J. Anderson, *Fundamentals of Aerodynamics*. New York, NY: McGraw-Hill, 2001.
- D. J. Tritton, “Experiments on the flow past a circular cylinder at low Reynolds numbers,” (English), *Journal of Fluid Mechanics*, vol. 6, no. 04, pp. 547–567, 1959.
- F. Kummer, “The BoSSS Discontinuous Galerkin solver for incompressible fluid dynamics and an extension to singular equations,” 2012.
- R. J. LeVeque, *Numerical methods for conservation laws*: Springer, 1992.
- M. N. Linnick and H. F. Fasel, “A high-order immersed interface method for simulating unsteady incompressible flows on irregular domains,” *Journal of Computational Physics*, vol. 204, no. 1, pp. 157–192, 2005.
- C. Liu, X. Zheng, and C. H. Sung, “Preconditioned Multigrid Methods for Unsteady Incompressible Flows,” *Journal of Computational Physics*, vol. 139, no. 1, pp. 35–57, 1998.
- M. Braza, P. Chassaing, and H. Ha Minh, “Numerical study and physical analysis of the pressure and velocity fields in the near wake of a circular cylinder,” (English), *Journal of Fluid Mechanics*, vol. 165, pp. 79–130, 1986.
- Madeleine Coutanceau and Roger Bouard, “Experimental determination of the main features of the viscous flow in the wake of a circular cylinder in uniform translation. Part 1. Steady flow,” (English), *Journal of Fluid Mechanics*, vol. 79, no. 02, pp. 231–256, 1978.
- S. Marella, S. Krishnan, H. Liu, and H. S. Udaykumar, “Sharp interface Cartesian grid method I: An easily implemented technique for 3D moving boundary computations,” *Journal of Computational Physics*, vol. 210, no. 1, pp. 1–31, 2005.
- Miyake, T, Sakamoto, Y, Tokunaga, H. and Satofuka, N, Ed, “*Numerical Solution of Incompressible Flow Using Two-Step, One-Stage Runge-Kutta Time Integration Scheme*,” 1992.
- S. C. R. Dennis and Gau-Zu Chang, “Numerical solutions for steady flow past a circular cylinder at Reynolds numbers up to 100,” (English), *Journal of Fluid Mechanics*, vol. 42, no. 03, pp. 471–489, 1970.
- B. R. Noack and Helmut Eckelmann, “A global stability analysis of the steady and periodic cylinder wake,” (English), *Journal of Fluid Mechanics*, vol. 270, pp. 297–330, 1994.
- A. ROSHKO, “ON THE DRAG AND SHEDDING FREQUENCY OF TWO-DIMENSIONAL BLUFF BODIES,” 1954.
- E. M. Saiki and S. Biringen, “Numerical Simulation of a Cylinder in Uniform Flow: Application of a Virtual Boundary Method,” *Journal of Computational Physics*, vol. 123, no. 2, pp. 450–465, 1996.
- M. Schäfer, *Computational Engineering - Introduction to Numerical Methods*. Berlin, Heidelberg: Springer-Verlag Berlin Heidelberg, 2006.

-
- Thomas Utz, “Validation of curved elements for incompressible viscous flow problems,” Master Thesis, Fachgebiet für Fluidodynamik, Technische Universität Darmstadt, Darmstadt, 2014.
- E. F. Toro, “A fast riemann solver with constant covolume applied to the random choice method,” (en), *International Journal for Numerical Methods in Fluids*, vol. 9, no. 9, pp. 1145–1164, 1989.
- E. F. Toro, *Riemann Solvers and Numerical Methods for Fluid Dynamics*: Springer, 2009.
- Z. J. Wang, K. Fidkowski, R. Abgrall, F. Bassi, D. Caraeni, A. Cary, H. Deconinck, R. Hartmann, K. Hillewaert, H. T. Huynh, N. Kroll, G. May, P.-O. Persson, B. van Leer, and M. Visbal, “High-order CFD methods: current status and perspective,” (en), *International Journal for Numerical Methods in Fluids*, vol. 72, pp. 811–845, 2012.
- C. H. Williamson, “The Existence of Two Stages in the Transition to Three-Dimensionality of a Cylinder Wake,” 1988.
- C. H. K. WILLIAMSON, “Oblique and parallel modes of vortex shedding in the wake of a circular cylinder at low Reynolds numbers,” (eng), *Journal of Fluid Mechanics*, vol. 206, pp. 579–627, 1989.
- C. H. K. WILLIAMSON, “Vortex dynamics in the cylinder wake,” (en), *Annual Review of Fluid Mechanics*, vol. 28, pp. 477–539, 1996.
- M. M. Zdravkovich, “DIFFERENT MODES OF VORTEX SHEDDING: AN OVERVIEW,” *Journal of Fluids and Structures*, vol. 10, no. 5, pp. 427–437, 1996.